Gastaldo, R.A., Neveling, J., Geissman, J.W., Kamo, S.L., and Looy, C.V., 2021, A tale of two Tweefonteins: What physical correlation, geochronology, magnetic polarity stratigraphy, and palynology reveal about the end-Permian terrestrial extinction paradigm in South Africa: GSA Bulletin, https://doi.org/10.1130/B35830.1.

Supplemental Material

Table S1. Paleomagnetic results from individual specimens, either as standard right cylinders or as packed ceramic cubes, collected at different stratigraphic levels in the Tweefontein and Tweefontein sections, Farm Tweefontein, Lootsberg Pass area, Eastern Cape Province, South Africa.

Figure S1. Transmitted light photomicrographs of two polished thin sections of the inferred volcanic ash deposit collected in the Tweefontein[2] section, prepared orthogonal to the orientation of deposit.

Figure S2. Scanning electron photomicrographs of selected areas of one of the polished thin sections of the inferred volcanic ash deposit collected in the Tweefontein[2] section, prepared orthogonal to the orientation of the deposit.

Figure S3. Orthogonal progressive demagnetization diagrams showing the end point of the magnetization vector plotted onto the horizontal (filled symbols) and vertical (open symbols) planes (NS-EW, EW-Up/Dn) for individual specimens from samples from selected sites sampled at the Tweefontein[1] and Tweefontein[2] sections that have been subjected to either progressive alternating field (AF) or thermal demagnetization.

Figure S4. Plots showing the acquisition of isothermal remanent magnetization (IRM) and backfield direct-field demagnetization for specimens from selected samples from sites in the Tweefontein[1] section.

Figure S5. Measurements of the bulk magnetic susceptibility as a function of heating and cooling for sample TW [1] 15_D, a greenish gray siltstone.

Figure S6. Measurements of the bulk magnetic susceptibility as a function of heating (to about 700^{o} C) and cooling for hematitic mudstone from ceramic cube sample TW [2] 2019_2e, collected at the locality of the TW [2] ash deposit.

Figure S7. An evaluation of the possibility of some magnitude of inclination shallowing, during depositional and post-depositional processes affecting the sequence of types of sedimentary rocks sampled in the Tweefontein[1] and Tweefontein[2] sections sampled.

Figure S8. Equal area projections of paleomagnetic directional data from selected sites at the Tweefontein[1] and Tweefontein[2] stratigraphic sections sampled.

Figure S9. Orthogonal progressive demagnetization diagrams showing the end point of the magnetization vector plotted onto the horizontal (filled symbols) and vertical (open symbols) planes (NS-EW, EW-Up/Dn) for individual specimens from independent samples from site TW1_19 (Tweefontein[1] section) that have been subjected to progressive thermal demagnetization.

Figure S10. Examples of anisotropy of magnetic susceptibility data from selected sites in the Tweefontein[1] (A) and Tweefontein[2] (B) sections.

A tale of two Tweefonteins: what physical correlation, magnetic polarity stratigraphy, and geochronology reveal about the end-Permian terrestrial extinction paradigm in South Africa

Robert A. Gastaldo[a*], **Johann Neveling**[b], **John W. Geissman**[c, d], **Sandra L. Kamo**[e] and **Cindy V. Looy**[f]

[a] Department of Geology, Colby College, Waterville, ME 04901 USA

[b] Council for Geosciences, Private Bag x112, Silverton, Pretoria, South Africa 0001

[c] Department of Geosciences, The University of Texas at Dallas, Richardson, TX 75080-3021 US

[d] Department of Earth and Planetary Sciences, University of New Mexico, Albuquerque, NM 87131-0001 USA

[e] Jack Satterly Geochronology Laboratory, Department of Earth Sciences, University of Toronto, Toronto, Canada M5S 3B1

[f] Department of Integrative Biology, Museum of Paleontology, University and Jepson Herbaria, University of California–Berkeley, 3060 Valley Life Sciences Building #3140, Berkeley, California 94720-3140 USA

Supplemental Information

Here we provide supplemental material related to the geochronology, paleomagnetism and rock magnetism components of this study. All of this material is presented with text supplemented by a series of figures and tables, with supporting captions, which provide a full interpretation of any results presented.

METHODS

U-Pb CA-ID-TIMS Analytical Methods

Zircon grains were pretreated by chemical abrasion to remove radiation-damaged and altered zones (Mattinson, 2005) by placing them in a muffle furnace at ~900° C for ~24-48 hours to anneal radiation damage. This treatment was followed by partial dissolution in 50% HF in Teflon dissolution vessels at 200° C for approximately 9-17 hours. Each zircon fragment was

cleaned in HNO_3 at room temperature and transferred to a miniaturized Teflon dissolution capsule (Krogh, 1973). Weights were estimated from grain measurements using photomicrographs. A mixed ^{205}Pb-$^{233-235}U$ spike was added to the Teflon dissolution capsules during sample loading ('ET535' EARTHTIME community tracer, see www.earth-time.org). Zircon was dissolved using ~0.10 ml concentrated HF acid and ~0.02 ml 7N HNO_3 at 200° C for 3-5 days, and re-dissolved overnight in ~0.15 ml of 3N HCl. Uranium and lead were isolated from the zircon solutions using anion exchange columns, deposited onto out-gassed rhenium filaments with silica gel (Gerstenberger and Haase, 1997), and analyzed with a VG354 mass spectrometer using a Daly detector in pulse counting mode. Corrections to the ^{206}Pb-^{238}U and $^{207}Pb/^{206}Pb$ ages for initial ^{230}Th disequilibrium in the zircon data have been made assuming a Th/U ratio in the magma of 4.2. All common Pb was assigned to the isotopic composition of the Pb procedural blank. Dead time of the measuring system for Pb and U was 16 ns and 14 ns, respectively. The mass discrimination correction for the Daly detector is constant at 0.05% per atomic mass unit. Amplifier gains and Daly characteristics were monitored using the SRM 982 Pb standard. Thermal mass discrimination correction for Pb is 0.10 % per atomic mass unit. Uranium fractionation was measured internally and corrected for individual blocks. Decay constants are those of Jaffey et al. (1971); ^{238}U and ^{235}U are 1.55125×10^{-10}/yr and 9.8485×10^{-10}/yr, respectively. Age calculations were done using an in-house program by D.W. Davis. All age errors quoted in the text and table, and error ellipses in the Concordia diagrams are given at the 95% confidence interval. Plotting and weighted mean age calculations were done using Isoplot 3.00 (Ludwig, 2003).

Magnetic Polarity Stratigraphy

Remanence measurements were made on either a 2G Enterprise, DC SQUID, three-axis pulse-cooled superconducting rock magnetometer, interfaced with an automated specimen handler and an on-line alternating field (AF) degausser system, or JR5A or JR6A AGICO spinner magnetometers. Because the principal magnetic phase in Tweefontein strata is magnetite, although hematite carries part of the remanence at some sites, as shown in the main

text and below, specimens from all sample sites were subjected to both thermal and alternating field (AF) demagnetization. Thermal demagnetization was carried out using one of three ASC TD48, dual zone thermal demagnetizers (internal ambient field < 10 nT), in a progressive fashion involving 20 to 30 steps to maximum laboratory unblocking temperatures of 680° C (±). AF demagnetization was carried out using the integrated 2G Enterprises AF demagnetization system, typically to peak fields of 90 to 120 mT.

Acquisition of isothermal remanent magnetization (IRM) and backfield demagnetization of saturation IRM utilized an ASC multi-coil impulse magnet system. Three component thermal demagnetization of IRM acquired in different DC fields followed the method of Lowrie (1990). Anisotropy of magnetic susceptibility (AMS) determinations were made using either an AGICO Inc. KLY-3S or a MFK1A automated magnetic susceptibility Kappabridges, the latter equipped with a 3-D specimen manipulator. All remanence measurements and demagnetization procedures were performed in a large (Lone Star State sized) magnetic shield (production #50) constructed by Lodestar Magnetics.

Results of progressive demagnetization were inspected using orthogonal demagnetization diagrams (Zijderveld, 1967), and the directions of magnetization components identified by the co-linearity of several demagnetization data points determined using principal components analysis (Kirschvink, 1980), mainly using the data examination and reduction software Remasoft (AGICO, Inc.). For most samples, demagnetization response is such that principal components analysis was applied to data unanchored to the origin, and maximum angular deviation (MAD) angles less than 15 were consistently obtained (Supplemental Information Table S1). Magnetization directions at the site level were estimated as mean directions using as many independent observations as accepted, following the method of Fischer (1953). These estimated site mean-magnetization directions are transformed into virtual geomagnetic poles (VGPs), relative to the time averaged paleomagnetic pole for southern Africa for latest Permian time, to infer the magnetic polarity stratigraphy of each section (Opdyke and Channell, 1996). Estimated paleomagnetic pole positions (e.g., Van der Voo, 1993; Torsvik et al., 2012, Muttoni et al., 2013) for Africa during the Late Permian/Early Triassic are such that the

direction of normal polarity magnetizations in these strata in the Groot Karoo, Eastern Cape Province of South Africa, should be of north–northwest declination and moderate/steep negative inclination. The present day field direction at the study locality (IGRF12 model), is quite similar, with a declination of -25.14˚ and an inclination of -64.56˚.

RESULTS

Fine-grained Lithofacies

In general, thick siltstone intervals appear massive in the field but occasionally expose primary structures that include micro-cross bedding and mm-scale lamination, more often when viewed in thin section (Gastaldo et al. 2014, 2020b). These features are independent of siltstone color, which ranges from olive (5Y 4/1) and light olive gray (5Y 6/1) and greenish gray (5GB 5/1), and variants thereof, to variants of grayish red (5R 4/2) and grayish brown (2.5Y 5/2; Fig 6D; Li et al., 2017; Gastaldo et al., 2019b). Mottling is grayish-red color variants with greenish-gray color variants. Although not ubiquitous, several intervals contain calcite-cemented, pale to moderate brown (5 YR 5/2–5 YR 4/4) or brownish gray (5YR 4/1) large concretions (10 to >50 cm diameter). These may occur isolated or amalgamated on one or more stratigraphic levels (Fig. 4C). Small, centimeter-scale pedogenic nodules encountered in situ in calcic Vertisols (Neveling et al., 2016a) and septarian nodules are rare. Three localities expose relatively thin (≤10 cm) beds of white (N9) or grayish/bluish white (5B 9/1), silicified siltstone or claystone or devitrified claystone (Fig. 6B–D). Silicified siltstone or claystone (porcellanite) consists of cm-scale thick, well cemented and laterally continuous beds that are more resistant to weathering and are prominent in outcrop. Devitrified claystone is highly weathered, resulting in a sticky (kaolinitic) texture on the outcrop surface. Floral and faunal evidence is most common in these fine-grained units.

U-Pb CA-ID-TIMS Analyses

Geochronology Supplemental Figure S1. (A–D) Transmitted light photomicrographs of two polished thin sections of the inferred volcanic ash deposit collected in the Tweefontein [2] section, prepared orthogonal to the orientation of deposit. (A, B) Uncrossed polars of one thin

section, two different magnetizations. (C, D) Separate thin section, uncrossed polars, two different magnifications. Note scale bars. Yellow circles highlight examples of flattened devitrified ash shards. Images taken using an Olympus BX51 with an Olympus DP 72 camera attachment.

Geochronology Supplemental Figure S2. (A–F) Scanning electron photomicrographs of selected areas of one of the polished thin sections of the inferred volcanic ash deposit collected in the Tweefontein [2] section, prepared orthogonal to the orientation of the deposit. Also show in selected frames are energy dispersive spectroscopy (EDS) spectra showing the elemental composition of some of the identified mineral phases present. Note scale bar for image size. Images collected using a JEOL STM-IT100.

Magnetic Polarity Stratigraphy

Paleomagnetism/Rock Magnetism Supplemental Figure S3. Orthogonal progressive demagnetization diagrams (parts A–D; Zijderveld, 1967) showing the end point of the magnetization vector plotted onto the horizontal (filled symbols) and vertical (open symbols) planes (NS-EW, EW-Up/Dn) for individual specimens from samples from selected sites sampled at the Tweefontein[1] and Tweefontein[2] sections that have been subjected to either progressive alternating field (AF) or thermal demagnetization. Selected demagnetization steps are shown for data points in the vertical position. Also shown are normalized intensity decay plots showing response to progressive AF or thermal demagnetization and stereographic projections of the magnetization vector measured at each step. Note that some of the demagnetization data shown in this figure are identical to those in Figure 13 of the main text.

Paleomagnetism/rock Magnetism Supplemental Figure S4. Plots showing the acquisition of isothermal remanent magnetization (IRM) and backfield direct-field demagnetization for specimens from selected samples from sites in the Tweefontein[1] section. In backfield demagnetization, the cross-over point provides the coercivity of remanence. The fact

that saturation or near- saturation is reached by 300 mT indicates that a cubic magnetic phase (magnetite/maghemite) is the principal magnetic phase present. This is consistent with the coercivity of remanence values below. Measurements conducted using an AGICO JR6A spinner magnetometer and magnetic fields imparted by an ASC Scientific multi-coil impulse magnetizer.

Paleomagnetism/Rock Magnetism Supplemental Figure **S5**. Measurements of the bulk magnetic susceptibility as a function of heating and cooling for sample TW [1] 15_D, a greenish gray siltstone. First two measurements shown are performed on a bulk sample in argon gas to a maximum temperature of 680° C. These experiments show the very slight decrease in susceptibility below 440° C, likely reflecting the breakdown of maghemite to hematite. At higher temperatures, a slight Hopkinson peak is demonstrated, revealing the presence of relatively coarse magnetite. This is followed by the major decrease in susceptibility below about 590° C, revealing the presence of nearly pure magnetite. The very minor susceptibility remaining at higher temperatures likely reflects a minor amount of hematite. The curves are irreversible, and show that a phase of increased susceptibility (perhaps maghemite) has been produced during the complete thermal heating. Remaining measurements are performed in air, and involve cycling of the same specimen to progressively higher and higher temperatures to monitor changes in magnetic mineralogy. The results of this experiment show no appreciable changes to the magnetic mineralogy as a function of progressive cycling to higher temperatures. Measurements conducted using an AGICO MFK1-A susceptibility instrument interfaced with a CS-4 heating system.

Paleomagnetism/Rock Magnetism Supplemental Figure **S6.** Measurements of the bulk magnetic susceptibility as a function of heating (to about 700° C) and cooling for hematitic mudstone from ceramic cube sample TW [2] 2019_2e, collected at the locality of the TW [2] ash deposit. Measurements of a bulk sample have been performed in air and in argon gas, and in each case the measurements are repeated on the same bulk sample, to evaluate the changes in

magnetic mineralogy after a first complete cycling. Initial runs, both in air and argon gas, show an increase then major decrease in susceptibility between about 160 and 380° C, followed by a major decrease in susceptibility below about 590° C (with a slight Hopkinson peak prior to that decrease, and thereupon the persistence of a very slight susceptibility to about 680° C. Both initial curves are irreversible, with a slight decrease in susceptibility in final cooling. We interpret this behavior to indicate the breakdown of maghemite to hematite in the heating curve, and then the Curie temperature of nearly pure magnetite is reached below 590° C, with remaining susceptibility reflecting the presence of hematite. In the second cycling, the heating/cooling curves are essentially reversible, and reveal the presence of a combination of thermally stable magnetite/maghemite as well as minor hematite as the remaining magnetic phases. Measurements conducted using an AGICO MFK1-A susceptibility instrument interfaced with a CS-4 heating system.

Paleomagnetism/Rock Magnetism Supplemental Figure S7. We evaluated the possibility of some magnitude of inclination shallowing, during depositional and post-depositional processes affecting the sequence of types of sedimentary rocks sampled in the Tweefontein[1] and Tweefontein[2] sections sampled. We carried out the now well-utilized elongation/inclination analysis first described by Tauxe and Kent (2004). We utilized demagnetization results, obtained with principal components analysis, from a total of 321 specimens from a total of some 285 independent samples. The distribution of data shown in Figure S6 does not provide a solution. The original inclination of the data set is 57.66°; and the range of bootstrapped confidence bounds is between 58.02° and 73.69°. There are a number of possible explanations for the "pathological" outcome of this analysis, including that the geomagnetic field has not been adequately sampled in this collection.

Paleomagnetism/Rock Magnetism Supplemental Figure S8. Equal area projections of paleomagnetic directional data from selected sites at the Tweefontein[1] and Tweefontein[2] stratigraphic sections sampled. In each projection, individual sample directions, all of which

are associated with maximum angular deviation (MAD) values less than 15°, are shown along with the estimated site mean direction (larger circle) and the projected cone of 95 percent confidence (dashed gray line). Sample directions are given in Supplemental Data Table 1.

Paleomagnetism/Rock Magnetism Supplemental Figure S9. Orthogonal progressive demagnetization diagrams (A–F; Zijderveld, 1967) showing the end point of the magnetization vector plotted onto the horizontal (filled symbols) and vertical (open symbols) planes (NS-EW, EW-Up/Dn) for individual specimens from independent samples from site TW1_19 (Tweefontein[1] section) that have been subjected to progressive thermal demagnetization. Selected demagnetization steps are shown for data points in the vertical projection. Also illustrated are normalized intensity decay plots showing response to progressive treatment and stereographic projections of the magnetization vector measured at each step. (G, H) Equal area projections of paleomagnetic data from Site Tw1_19; (G) shows first-removed vectors; (H) shows higher laboratory unblocking temperature magnetizations along with projected maximum angular deviation (MAD values) for each specimen result. (I–T) Same as (A–F) but for specimens from independent samples from site Tw1_20 (Tweefontein[1] section). (U–W) Equal area projections summarizing demagnetization results. (U) directions of linear segments and projected maximum angular deviations for each specimen result, with large circle as the estimated mean direction of the population; open (closed) symbols represent projections on the upper (lower) hemisphere. (V) great circles (dashed on upper hemisphere) defined by demagnetization trajectories for some of the specimens from site TW1_20, showing estimated mean normal to the great circles and confidence limit. (W) combination of linear segments and great circles showing locations of end points along great circle trajectories. Note that some of these data are shown in Figure 18 in the main text.

Paleomagnetism/Rock Magnetism Supplemental Figure S10. Examples of anisotropy of magnetic susceptibility data from selected sites in the Tweefontein[1] (A) and Tweefontein[2] (B) sections. For each site, the stereographic projection shows the principal susceptibility axes for

each specimen measured (lower hemisphere projections) and the mean principal susceptibility directions for the site. In addition, the anisotropy parameter P (degree of anisotropy, P = Kmax/Kmin), is plotted vs. bulk susceptibility for each specimen measured. Also shown is a plot of the AMS shape parameter T (T=[lnF-lnL/lnL + lnF]) versus the anisotropy parameter P for each specimen. The data from each site show a fabric that is typical of very fine grained detrital sedimentary rocks, with the minimum susceptibility axis essential vertical and well-grouped.

SUPPLEMENTAL MATERIAL REFERENCES

FISHER, R.A., 1953, Dispersion on a sphere: Proceedings of the Royal Society of London, v. A217, p. 295–305.

GERSTENBERGER, H., AND HAASE, G., 1997, A highly effective emitter substance for mass spectrometric Pb isotope ration determinations: Chemical Geology, v. 136, p. 309–312.

JAFFEY, A.H., FLYNN, K.F., GLENDENIN, L.E., BENTLEY, W.C., AND ESSLING, A.M., 1971, Precision measurement of half-lives and specific activities of 235U and 238U: Physics Review, v. 4, p. 1889-1906.

KIRSCHVINK, J.L., 1980, The least squares line and plane and the analysis of paleomagnetic data: Geophysical Journal of the Royal Astronomical Society, v. 62, p. 699-718.

KROGH, T.E., 1973, A low contamination method for hydrothermal decomposition of zircon and extraction of U and Pb for isotopic age determinations: Geochimica Cosmochimica Acta, v. 37, p. 485-494.

LUDWIG, K.R., 2003, User's manual for Isoplot 3.00: A geochronological toolkit for Microsoft Excel: Berkeley Geochronology Center, Special Publication, v. 4, p. 1-71.

MATTINSON, J.M., 2005, Zircon U/Pb chemical abrasion (CA-TIMS) method; combined annealing and multi-step partial dissolution analysis for improved precision and accuracy of zircon ages: Chemical Geology, v. 220, p. 47-66.

MUTTONI, G., DALLANAVE, E., AND CHANNELL, J.E.T., 2013, The drift history of Adria and Africa from 280 Ma to Present, Jurassic true polar wander, and zonal climate control on Tethyan sedimentary facies: Palaeogeography, Palaeoclimatology, Palaeoecology, v. 386, p. 415-435.

OPDYKE, N.D., AND CHANNEL, J.E.T., 1996, Magnetic Stratigraphy: San Diego, Academic Press, 346 p.

TAUXE, L, AND D.V. KENT, 2004, A simplified statistical model for the geomagnetic field and the detection of shallow bias in paleomagnetic inclinations: Was the ancient magnetic field dipolar?: *in* Channell, J.E.T. Kent, D.V., Lowrie, W., and Meert, J.G., eds. Timescales of the Paleomagnetic Field: American Geophysical Union Monograph 145, p. 101-115.

VAN DER VOO, R., 1993, Paleomagnetism of the Atlantic, Tethys, and Iapetus Oceans: Cambridge, Cambridge University Press, 411 p.

Supplementary Table 1. Paleomagnetic results from individual specimens, either as standard right cylinders or as packed ceramic cubes, collected at different stratigraphic levels in the Tweefontein [1] and Tweefontein [2] sections, Farm Tweefontein, Lootsberg Pass area, Eastern Cape Province, South Africa.

Specimen	C1, Decl.[a]	C1, Incl.[b]	Demag. Int.[c]	MAD[d]	C2, Decl.[a]	C2, Incl.[b]	Demag. Int.[c]	MAD[d]
TW [1] _1Aa	349.5	-37.2	466-575	5.2				
Bb	345.2	-60.2	433-555	9.2				
Ca	342.4	-50.5	422-565	6.9				
Cb	333.6	-52.8	*21-71*	4.0				
Da	350.8	-49.8	444-586	5.2				
Dc	334.7	-53.6	422-575	4.7				
Ea	337.7	-53.3	422-573	5.9				
Ee	348.4	-52.5	477-584	4.4				
Fb	324.6	-51.8	422-575	5.3				
Ga	353.5	-47.8	422-575	9.1				
Hb	350.3	-43.5	500-595	5.2				
Ia	356.7	-48.2	422-565	8.6				
Je	349.3	-51.6	422-573	4.7				
TW [1] _2Aa	349.9	-56.3	396-544	8.1				
Ac	346.7	-62.7	422-566	13.1				
Ba	338.8	-51	*26-73*	2.3				
Ca	328.6	-50.7	444-573	5.3				
Db	358.6	-54.5	*15-75*	2.3				
Ea	350.1	-51.8	*16-46*	2.6				
Ec	354.1	-51.6	477-584	5.0				
Fc	321.5	-45.4	466-595	6.3				
Ga	319.2	-52	466-566	6.4				
Ia	331.3	-58.5	396-544	7.8				
Id	324.4	-46.7	477-572	4.9				
Jb	338.9	-42.9	*20-80*	8.4				
Jc	335.5	-47.4	422-595	16.3				
TW [1] _3Aa	359.6	-28.2	422-555	1.1				
Ab	320.6	-63	388-522	6.9				
Bb	333.1	-58.5	388-544	3.8				
Bbb	328.2	-50.7	388-555	6.4				
Bc	319.9	-52.5	377-533	5.4				
Ca	314.7	-60.4	366-511	6.1				
Cc	322.6	-47.4	388-544	8.7				
Da	320.9	-55.9	*21-54*	4.6				
Db	332.3	-64.8	422-555	9.4				
Dd	334.7	-64.7	433-533	5.6				
Fa	327.9	-64.1	*34-86*	5.7				
Ga	340.7	-48.9	422-511	6.7				
Gb	343.7	-62.4	*21-80*	2.5				

Ha	319.3	-56.2	388-568	5.0
Hc	337.9	-58.6	388-522	4.2
TW [1] _4Aa	327.8	-48.8	344-544	12.4
Ab	324.9	-61	*18-98*	2.5
Ba	337.9	-53.5	333-488	3.5
Cb	325.6	-53	377-511	9.5
Da	329.9	-60.9	366-538	9.0
Dc	329.3	-59.3	344-500	3.3
Eb	327	-53.5	344-544	11.5
Fb	308.3	-55.8	377-511	13.1
Gb	313.3	-58.2	344-500	4.3
Gd	328.7	-60.3	325-477	4.1
Ha	315.8	-60	*34-102*	2.0
Ia	336.8	-57	366-511	5.8
Ja	327.7	-60.2	300-477	4.4
TW [1] _5Ac	347.1	-62.8	422-544	10.2
Ba	349.6	-51.5	*9-25*	6.1
Cb	21.2	-62.4	388-522	7.8
Cc	1.1	-52.4	366-538	8.2
Da	41.5	-69	388-566	10.2
Db	26.4	-67.8	*24-54*	4.7
Ea	351.4	-55	388-555	4.0
Eb	94.4	-69.6	422-575	12.4
Fa	336.9	-59.7	*21-82*	3.1
Fb	345.8	-56.5	388-544	5.9
Ga	326.4	-62	388-566	13.4
Gb	342.9	-56.1	*22-85*	3.4
Ia	353.9	-60.5	388-568	7.5
Ib	351.2	-58.2	366-511	4.6
Jb	336.2	-53.8	366-538	4.8
Jc	342	-59.4	433-533	8.1
TW [1] _6Ac	337.5	-50	377-522	6.3
Cb	29.4	-66	377-555	5.7
Da	4.8	-47.7	*33-82*	3.8
Fa	325.9	-73.3	300-522	2.7
Ja	353.4	-52.9	377-555	6.4
TW [1] _7 Ba	309.8	-54.4	411-560	10.1
Ea	335.2	-67.6	411-560	2.2
Fa	340.3	-53	366-540	7.7
Ha	332.7	-65.3	411-594	7.3
Hb	319.9	-73	*38-86*	15.8
TW[1] 8Ba	338.5	-58.8	*40-83*	6.0
Da	323.2	-63.1	411-540	5.8
Ga	52.5	-40.3	411-560	3.9
Ha	338.1	-55.2	411-573	5.9
Ia	339.3	-57.4	411-560	4.0
TW[1]_9Aa	14.8	-51.3	*30-76*	2.5
Ea	319.9	-62.5	435-570	3.4

Ga	322.9	-67.7	435-570	16.5
Ha	329.1	-57	435-570	5.7
Ia	322.2	-64.8	435-570	4.1
TW[1]_10Aa	327.9	-56.9	377-570	9.9
Bb	79	-49.1	*56-80*	5.5
Da	309.3	-58.6	300-588	6.2
Ka	335.7	-60.3	377-555	8.7
Kc	320.3	-53.8	444-568	12.4
TW [1]_11Aa	333.4	-58.9	444-576	2.3
Bb	328.5	-58.9	435-588	2.2
Db	327.3	-62.7	*50-86*	0.4
Fa	330.5	-57.1	435-588	1.9
Ha	324.9	-59.6	435-588	1.4
Ia	333.5	-52.2	435-588	3.6
TW[1]_12Aa	291.5	-46.6	488-586	1.2
Cb	296.1	-40.1	411-560	4.2
Dc	294.9	-25	510-583	2.0
Ea	323	-18.1	505-580	2.4
Ebb	328.7	-62.5	*43-85*	0.7
Je	336.3	-11.7	555-600	2.5
TW[1]_13Bb	341.5	-55.8	511-600	0.9
Bc	330.4	-57.2	466-573	2.5
Ca	335.5	-56.1	*18-36*	0.8
Cb	329.4	-56.2	411-594	3.5
Dc	340.7	-56.9	505-580	3.3
Ea	339	-54.4	444-568	4.6
Eb	335.5	-55.2	477-584	2.6
Ga	336.9	-34.6	510-583	2.8
Gb	332.4	-62.5	411-573	1.5
TW[1]_14Ac	345.1	-54.9	377-555	3.7
Ca	332.8	-55.9	411-560	4.8
Db	332	-55.8	411-560	9.3
Dc	332.7	-56.5	*18-55*	0.6
Ebb	318.2	-47.6	411-573	5.8
Ga	335.5	-58.8	444-568	1.7
Hd	351.7	-54.7	477-572	9.4
Ja	292.8	-68.2	*42-97*	0.7
Jb	290.5	-68.5	411-620	3.4
TW[1]_15Cb	6.7	-52.8	25-80	1.1
Db	326.5	-62.1	411-573	6.5
Ebb	330.9	-59.9	444-620	8.3
Fb	328.9	-64.8	366-560	3.3
Ha	344.8	-54.8	411-620	5.0
Iz	343.4	-57.6	477-572	3.5
Jc	345.8	-61.2	477-584	2.8
TW[1]_16Aa	338.5	-55.6	*32-108*	1.2
Fa	341.4	-56.5	444-585	4.9
Ga	334.1	-59	396-561	10.7

Ha	341.6	-56.6	444-576	5.0
Ia	340.6	-57.9	444-573	4.0
TW[1]_17Da	347.6	-58.9	444-573	3.9
Ea	342.3	-53	444-576	4.5
Eb	351.5	-52.8	444-585	5.5
Fc	351.9	-59.5	*30-80*	1.3
Gb	350.1	-51	444-573	7.8
Ha	346.4	-46.2	444-561	6.1
TW[1]_18Ba	345.6	-43.1	488-573	6.6
Ca	335.6	-53.7	365-553	2.4
Cb	336.2	-53.5	416-562	6.6
Db	317.2	-55.3	365-553	3.3
Ebb	336.4	-60	365-553	2.3
Fa	332.4	-53.6	444-561	2.4
Ga	333.5	-56.5	396-561	1.5
Ha	331.6	-56	*30-65*	0.6
Ia	356.5	-59.4	396-544	8.9
TW[1]_19Aa	328.2	-52.1	173-416	1.8
Cb	344.7	-57	169-368	6.8
Da	330.1	-51.5	300-505	3.6
Daa	108.2	53.1	541-562	20.0
Db	324.8	-51.5	300-505	5.1
Ebb	330.5	-59.2	344-533	1.7
Ga	330.5	-55.8	411-533	3.9
Hc	335.8	-53.9	*36-91*	0.3
Ia	335.8	-54.2	300-505	4.7
Iaa	354.3	-52.4	411-533	6.6
Ja	338.4	-59.5	322-480	2.7
Ka	7.6	-60	388-533	3.6
TW[1]_20Ab	337	-56.2	210-466	3.0
Bc	345.1	-56.8	300-505	4.8
Db	329.4	-58.8	300-460	2.6
Eb	335	-58.6	*20-54*	3.2
Ga	342	-49.5	300-505	6.0
Gb	339.8	-63.6	344-500	6.8
Ia	328.4	-58	285-480	7.0
Ja	345.6	-50.9	400-540	6.7
Ka	329.8	-56	388-533	7.9
Kc	346.7	-56.7	277-466	3.1
La	329.6	-58.5	300-505	2.6
Mb	338.7	-53.5	285-480	7.2
TW[1]_21Bb	336.7	-56.9	*32-68*	4.9
Fa	348.3	-65.1	400-540	4.7
TW[1]_22Aa	337.7	-62.1	222-300	0.2
Ea	341.5	-64.9	222-300	0.3
Ga	338.8	-61.4	320-440	1.5
Ia	339.9	-62.3	222-300	0.4
Ib	337.3	-66.2	36-76	2.5

Ja	244.3	-77.1	222-377	1.0
TW [1] _23ACb	0.6	-76.8	169-285	7.0
Db	348.4	-61.6	*24-52*	10.9
Ha	346.1	-65.6	285-441	19.4
Fb	94.5	-68.9	400-569	8.5
TW[1] _23BEb	337.6	-37.8	285-441	6.7
Fb	53.3	-49.6	*20-48*	4.4
Fc	64.1	-62.9	366-525	17.5
Ia	353.8	-53.1	222-441	18.2
Ib	329.6	-66.3	303-500	14.8
Ib	324.5	-56.2	320-519	10.5
Jb	350.5	-60.3	303-525	11.0
TW[1] _24Aa	325.5	-60.1	368-557	5.6
Bb	319.5	-55.7	344-555	6.8
Da	338.5	-79.6	400-555	5.0
Ea	332.8	-64.2	*23-63*	3.1
Fb	342.8	-60.8	344-500	6.1
Hb	356.7	-58.7	411-533	8.8
TW[1] _25Cb	14.4	-47.8	322-535	12.7
Da	24.3	-43.7	400-569	7.0
Eb	326.9	-53	344-555	12.
Fa	302.2	-59.7	*26-74*	5.1
Ha	326.8	-66	368-568	4.8
Hb	16.2	-65.5	277-555	10.6
Ia	22.8	-64.9	344-572	13.1
TW[1] _26Ga	328.5	-56.6	322-535	2.3
Ia	340.9	-52.7	400-569	4.8
TW[1] _27Aa	340.6	-54.3	*39-87*	6.6
Ca	4.3	-59.7	400-555	5.9
Db	349.9	-35.8	411-595	7.5
Ec	346.9	-55.7	411-533	3.6
Gb	342.2	-55.9	344-500	1.5
TW[1] _28Eb	35.4	-62.7	440-540	2.4
Fb	316.2	-55.8	*38-80*	3.2
Ga	322.2	-56.9	396-544	4.0
Ha	355.8	-42.5	444-544	2.6
Ia	326.3	-56.8	444-544	6.8
Ja	329.4	-71.3	444-544	4.6
TW[1] _29Bb	4.4	-50	422-525	2.8
Cb	345.6	-55.8	366-545	4.6
Ea	349.9	-52.9	*15-40*	1.2
Fb	337.1	-58.7	422-556	6.4
Gb	330.1	-55.5	400-519	4.1
TW[1] _30Bb	328.9	-38.5	466-574	2.8
Cc	335.5	-40.6	466-565	7.5
Da	338.2	-38.1	440-569	6.3
Jb	330.1	-64.3	*27-55*	3.5
Jc	309.2	-72.7	466-565	3.1

Ka	292.9	-79.2	466-565	5.8
TW[1]_31Bb	345	-59.1	422-556	5.3
Fa	335.7	-61.8	233-366	2.9
Gb	353.8	-58.8	*25-75*	3.5
TW [1]_32Fa	343	-65.7	*24-54*	2.8
33Db	334.7	-49.9	*30-58*	3.1
Ea	336	-46.5	422-556	6.7
Ec	333.9	-39.7	*27-65*	6.4
Fc	351.9	-50.8	440-582	10.7
Ga	325.1	-40.5	422-545	9.4
Hb	334.7	-51	422-556	6.3
Ib	45.7	-59.9	*28-66*	10.6
Ic	325.5	-51.9	466-574	9.1
TW [1]_34Ba	328.6	-54.8	366-545	13.4
Cc	359.8	-39.5	400-555	10.3
Ga	315.2	-50.2	422-525	6.9
Ic	337	-46.5	24-60	3.4
TW [1]_35Cb	91.5	-77.5	475-620	5.2
Db	339.9	-53.3	18-58	2.6
Ea	348.6	-64.2	466-590	12.1
Fa	301.2	-58.4	422-581	8.8
Ga	325.2	-38.8	466-556	4.9
TW [1]_36Ga	347.4	-49.6	422-538	2.4
Gb	11.9	-50.6	440-569	4.6
Hc	308.3	-49.1	*31-71*	4.1
Ia	312.6	-40.7	477-565	1.9
Ja	351	-20.6	400-569	0.9
TW [1]_37Eb	338.6	-62.3	*38-86*	4.4
Ia	325.9	-56.1	400-555	7.6
TW [1]_38Ab	321.2	-53.3	277-466	8.1
Fa	341	-61.1	277-533	9.5
Gb	313.2	-18.1	466-555	15.2
Ha	42.2	-64.5	260-475	10.1
Ic	307	-46.9	365-495	8.0
Ja	333.2	-49.1	*19-43*	10.4
TW [1]_39Ba	343.1	-75.8	440-582	0.5
Bb	24	-76	466-582	1.2
TW [2]_40Aa	301.6	-55.1	350-565	2.1
Ba	314.9	-46.9	*31-80*	0.8
Ca	294.9	-54.8	400-565	4.8
Ea	283.6	-57.3	350-565	8.2
Ia	303.7	-57.0	400-565	4.6
TW [2]_41Aa	316.1	-57.5	343-528	1.9
Ba	308.5	-60.2	289-507	1.8
Ca	322.2	-57.7	*25-83*	1.4
Da	319.3	-76.1	350-565	6.0
Ga	341.2	-64.8	198-507	5.8
Ha	344.8	-60.8	400-574	3.8

TW [2] _42Aa	334.2	-64.2	350-565	8.3
Ab	315.3	-52.9	289-507	5.8
Bb	307	-54.8	289-528	4.2
Ca	349.6	-61.6	300-565	6.5
Cc	306.0	-55.4	289-507	8.1
Ea	331.9	-62.4	350-565	3.7
Eb	329.4	-61.6	300-565	6.5
Fa	329.6	-62.3	23-80	2.0
Ga	308.5	-61.9	244-507	3.5
Ha	340.1	-73.4	300-565	8.6
Ia	333.2	-62.5	350-565	5.7
Ka	294.4	-58.7	300-565	5.4
TW [2] _43Aa	315.3	-55.5	244-507	5.5
Ba	317.8	-52.9	289-528	3.4
Da	326.5	-64.6	*20-90*	1.7
Db	327.9	-60.2	350-573	2.9
Ea	321.6	-63.1	300-565	6.8
Eb	328.4	-59.5	350-573	5.8
Ga	331.8	-60.2	244-528	4.0
Ha	328.4	-57.0	300-565	3.8
TW [2] _44Ab	257.4	-45.9	350-573	6.8
Ba	282.6	-28.2	400-573	7.3
Ca	279.9	-31.2	350-565	10.0
Cb	330.8	-52.8	*23-85*	3.6
Da	314.1	-48.9	300-565	6.3
Ea	299.4	-64.6	350-565	14.6
Fb	339.1	-25.3	300-573	9.3
Ga	339.8	-21.2	350-565	11.1
TW [2] _45Aa	314.4	-61.7	391-557	2.2
Ba	336.8	-1.2	350-565	5.1
Ea	274.7	-36.4	300-565	4.6
Eb	307.9	-59.9	391-557	3.2
Fa	336.1	-49.9	391-557	6.3
Ga	317.3	-37.5	300-565	10.1
TW[2] _46Aa	305.2	-20.3	300-565	7.7
Cc	291.9	-28.3	350-565	3.8
Da	284.8	-29.2	300-565	3.7
Ea	305.6	-13.1	300-565	3.9
Fa	308.3	-12.1	350-565	2.7
TW [2] _47Ba	279.2	-32.6	300-565	10.6
Bb	317.7	-60.0	289-528	3.0
Ca	288.1	-33.0	300-545	6.0
Ea	319.7	-57.8	343-528	2.7
Fa	282.9	-67.2	300-565	5.2
Ga	279.6	-40.5	300-545	6.0
Ha	279.5	-36.1	350-545	4.2
Hb	326.6	-54.1	343-528	3.3
TW [2] _50Aa	285.9	-28.2	350-573	7.8

Cb	324.8	-55.9	*23-76*	8.2
Fb	159.7	-8.6	350-565	4.1
Ja	261.7	-54.6	350-565	10.9
Jb	267.6	-49.3	400-573	4.6
TW [2] _51Aa	333.6	-61.2	*38-86*	2.4
TW [2] _56Db	309	-46.7	391-557	5.7
Ea	332.5	-63.1	*35-90*	2.6
Eb	327.2	-53.7	333-557	3.3
Fa	317.5	-52.5	391-557	5.0
Gb	308.8	-54.7	333-557	2.9
TW [2] _57Ga	321.1	-56.9	*27-91*	2.3
TW [2] _58Ab	326.4	-57.6	333-557	2.1
Cb	330.5	-59	333-557	5.1
Ga	339.4	-58.7	391-557	4.6
Ha	353.2	-65.6	*27-83*	1.8
TW[2] _59Aa	315.8	-8.6	350-578	4.0
Ca	314.7	-7.0	350-565	4.3
Ea	310.5	-11.3	400-578	4.3
Ha	313.9	-9.4	350-578	3.3
Ka	329.2	-13.2	400-578	7.9
TW[2] _62Aa	290.3	-23.6	350-573	9.9
Ca	329.6	-16.7	400-573	10.0
Fa	335.9	-31.4	350-573	7.7
Ha	342.2	-27.7	300-565	8.0
Ia	333.2	-32.2	350-565	5.7
TW[2] _63 Ca	349.1	-60.0	350-565	5.3
Db	270.2	-56.1	400-573	9.1
Ga	320.8	-21.2	350-573	11.0
TW [2] _64Aa	302.6	-22.0	350-565	7.0
Ab	333.9	-60.3	*14-77*	2.6
Ba	305.4	-33.7	400-573	8.0
Ca	304.9	-20.6	400-565	10.4
Db	308.1	-28.9	400-565	10.9
Ea	296.1	-2.4	425-565	8.7
Fa	307.1	-24.3	400-565	11.9
TW [2] _65Aa	333.5	-54.6	391-557	6.9
Ba	339.1	-31.5	400-565	14.7
Cb	333.1	-59.9	26-91	2.4
Da	333.3	-32.2	350-565	3.7
Ea	336.6	-26.9	350-565	4.9
Fa	341.4	-46.3	400-565	6.7
Fb	346.9	-54.9	281-528	7.2
Ga	341.3	-69	333-528	4.3
Ia	336.4	-58.6	400-573	5.4
Ib	337.1	-61	391-548	4.3
TW [2] _66Aa	320.2	-72	*19-72*	3.9
TW [2] _67Aa	327.8	-49.6	481-664	1.8
Ca	327.8	-52.1	530-680	1.9

Ea	324.6	-56.9	530-675	5.5
Fa	329.5	-54	507-675	3.6
Ga	326.9	-55.9	550-680	3.3
TW ^{2}_68Aa	307.6	-55.8	530-675	4.6
Ba	319.2	-59.7	507-664	3.6
Ca	310.1	-42.6	507-670	3.6
Da	308.1	-53	550-670	3.8
Ga	358.1	-56.7	550-675	3.6
TW ^{2}_69Ba	317.8	-58.2	550-670	1.9
Da	320.4	-62.1	570-675	4.2
Ea	322.5	-60.4	530-664	4.0
Eb	326.7	-59.9	565-675	3.1
TW ^{2}_2019_1A	332.2	-46.1	573-678	2.9
TW ^{2}_2019_1B	32.3	-41.9	497-671	3.6
TW ^{2}_2019_1C	313.7	-68.3	573-658	14.5
TW ^{2}_2019_1D	40.7	-65.0	448-658	2.7
TW ^{2}_2019_1E	353.2	-58.5	402-671	3.2
TW ^{2}_2019_2B	5.5	-50.7	402-638	2.2
TW ^{2}_2019_2C	23.0	-53.8	448-638	3.4
TW ^{2}_2019_2D	352.8	-59.2	448-658	2.3
TW ^{2}_2019_2E	341.7	-44.8	448-651	2.0
TW ^{2}_2019_3A	300.0	-49.8	497-657	2.1
TW ^{2}_2019_3B	0.4	-54.3	497-671	2.2
TW ^{2}_2019_3C	316.5	-57.6	497-678	2.4
TW ^{2}_2019_3D	7.5	-48.4	497-671	1.0

Notes:

All data expressed in geographic coordinates.

a) declination, in degrees east of north, of the first-removed component of remanence(if any).
b) inclination, in degrees positive downwards and negative upwards, of the first-removed component of remanence (if any).
c) Laboratory unblocking temperature interval (in ^{o}C) or range of peak alternating fields (AF) (in mT) (*shown in italics*) over which first- or second- removed component is unblocked.
d) Maximum angular deviation (in ^{o}) result for first- or second-removed remanence component; **always determined using free-floating lin**es, never anchored to the origin.
e) Declination, in degrees east of north, of the second-removed component of remanence.
f) Inclination, in degrees positive downwards and negative upwards, of the second-removed component of remanence.

Fig. SI1

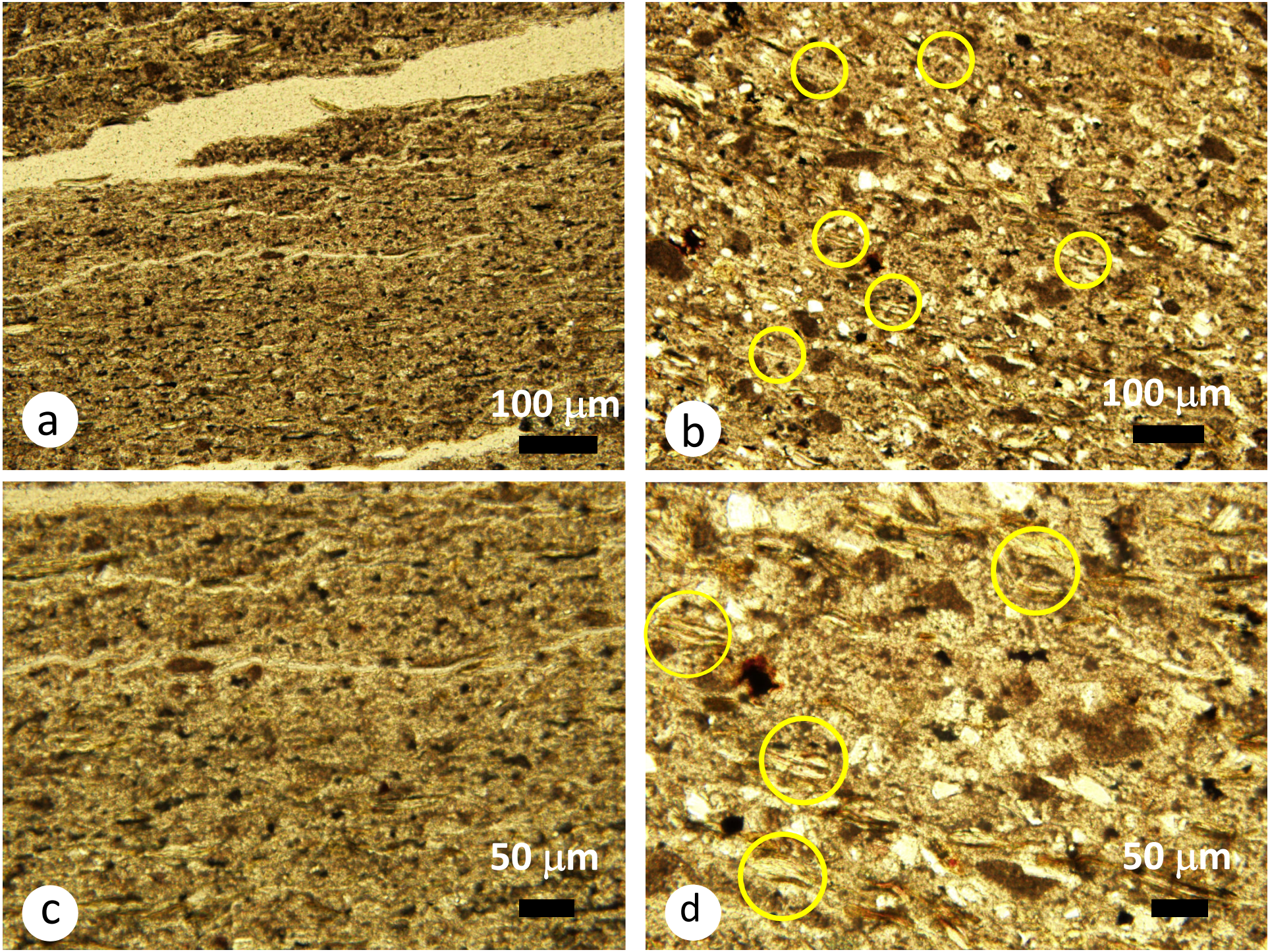

Fig. SI2

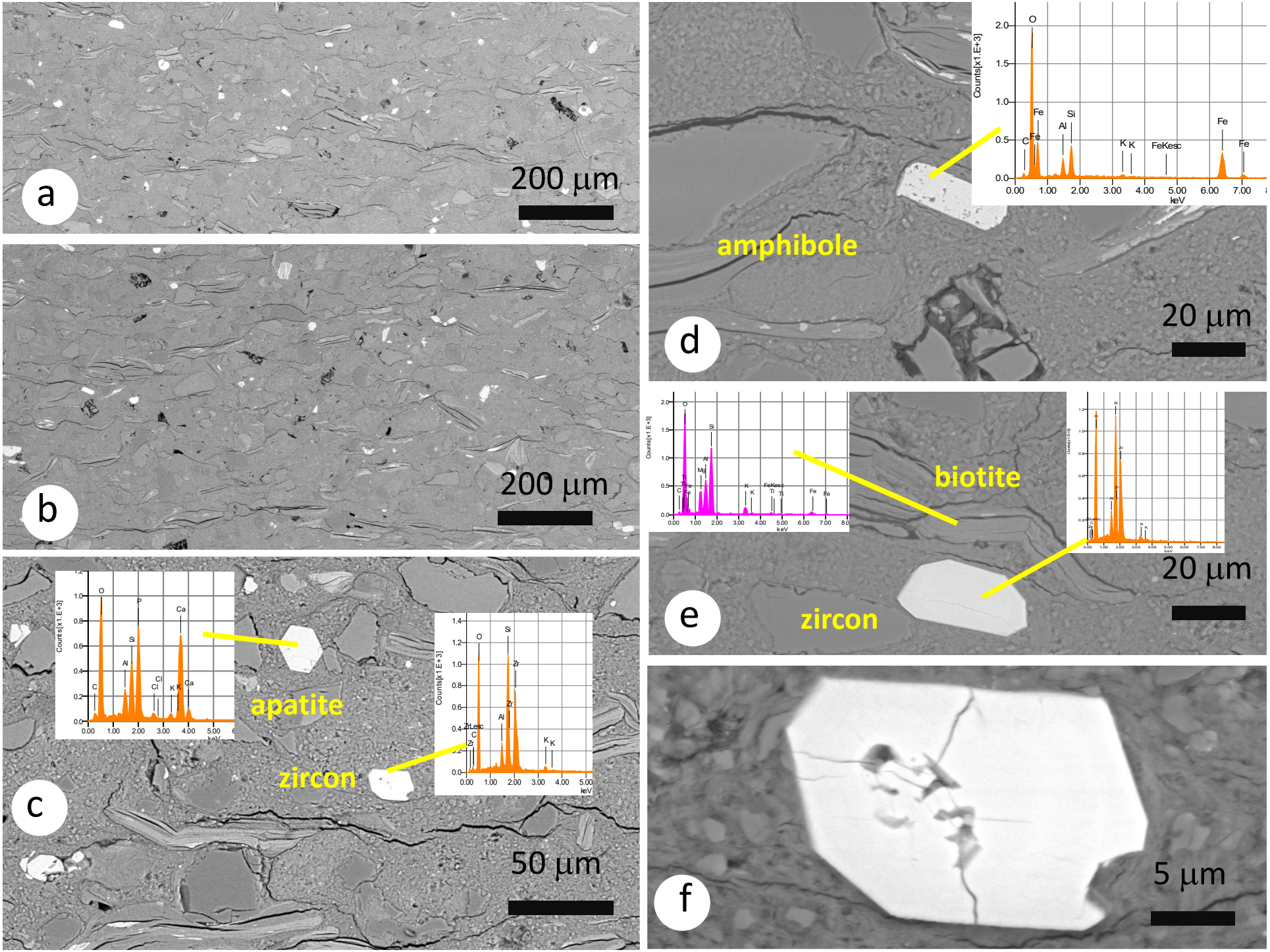
a
200 µm
b
200 µm
c
apatite
zircon
50 µm
d
amphibole
20 µm
e
biotite
zircon
20 µm
f
5 µm

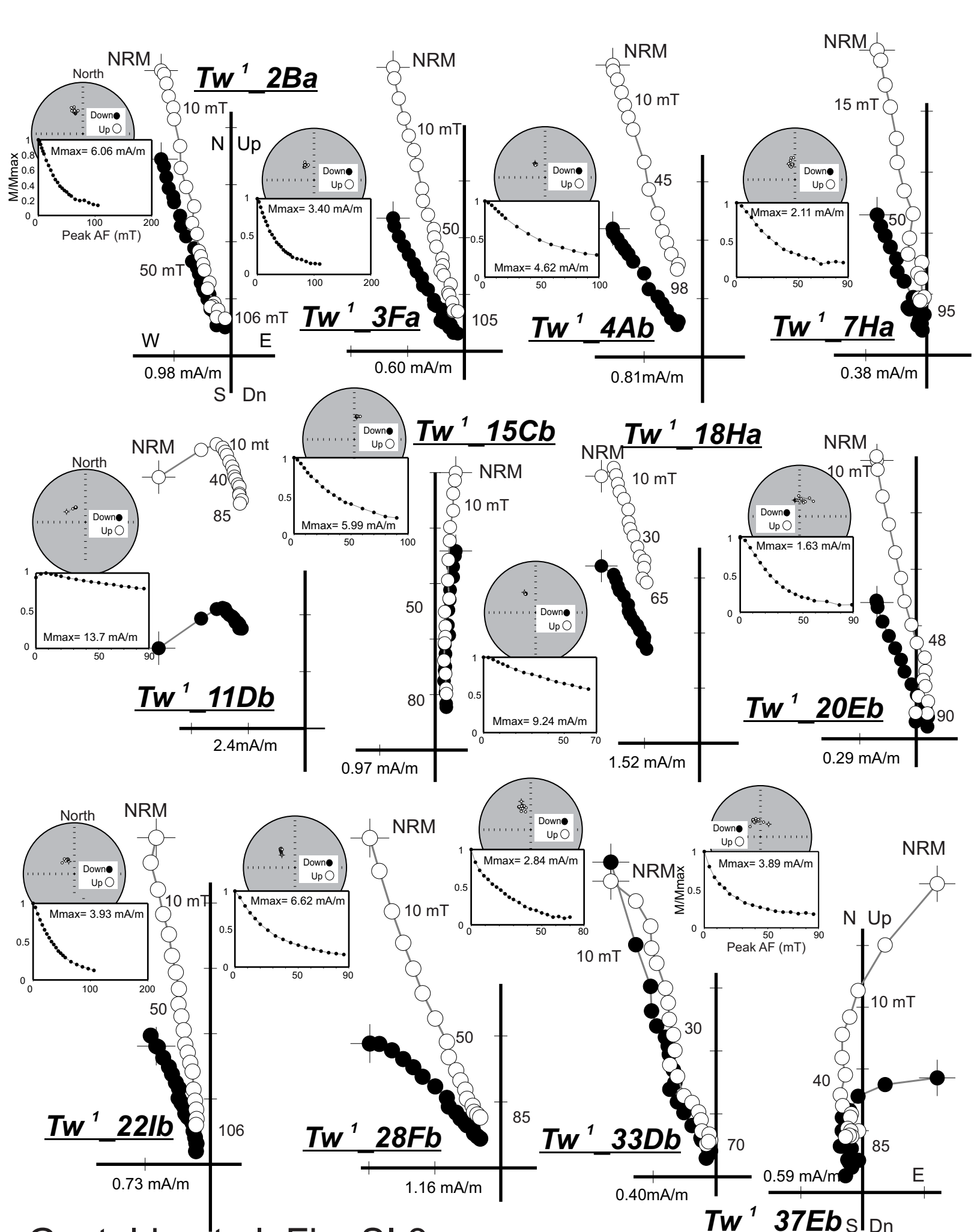

Gastaldo et al. Fig. SI 3

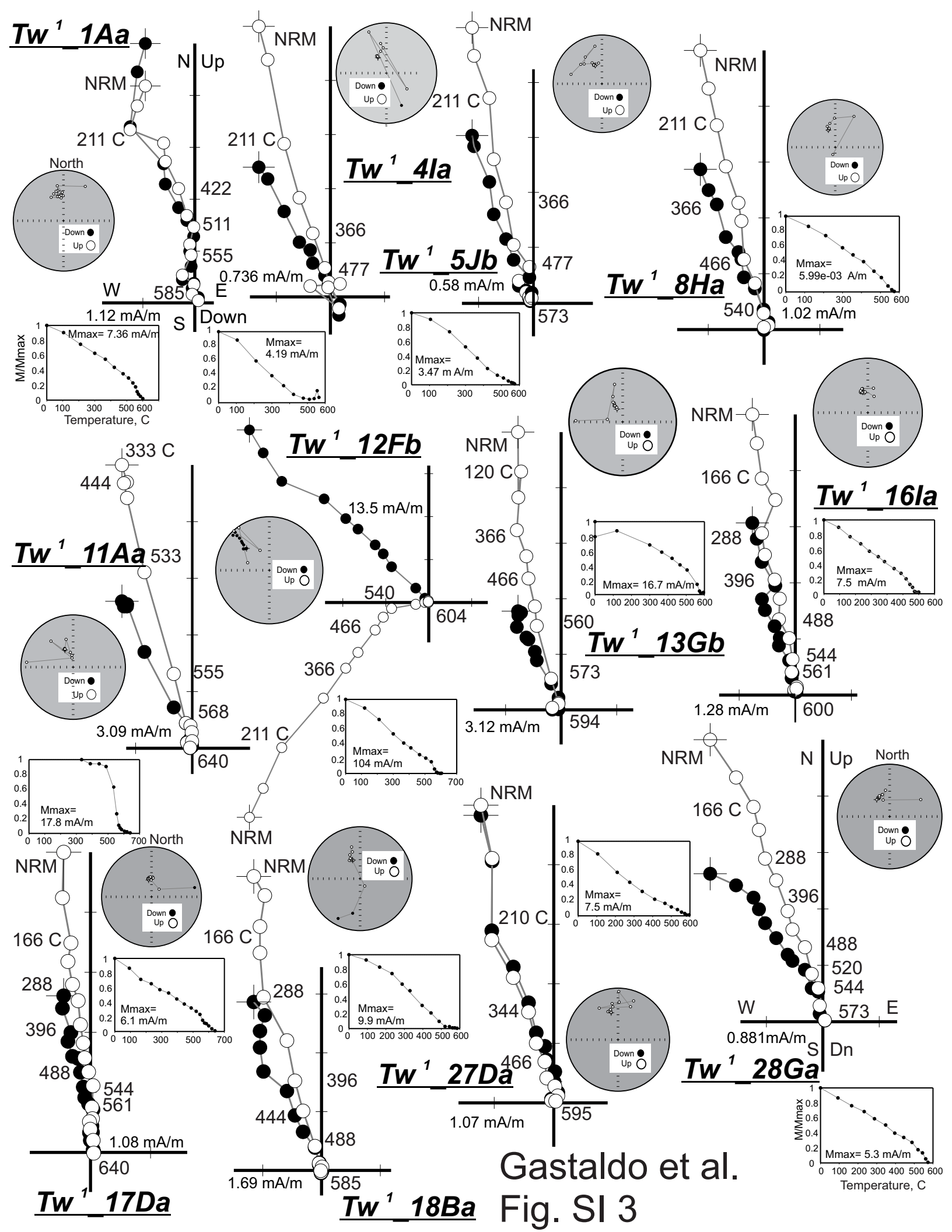
Tw¹_1Aa
NRM
211 C
422
511
555
585
N Up
W E
S Down
1.12 mA/m
Mmax= 7.36 mA/m
M/Mmax
Temperature, C
North
Down
Up
Tw¹_4Ia
NRM
211 C
366
477
0.736 mA/m
Mmax= 4.19 mA/m
Tw¹_5Jb
NRM
211 C
366
477
573
0.58 mA/m
Mmax= 3.47 m A/m
Tw¹_8Ha
NRM
211 C
366
466
540
1.02 mA/m
Mmax= 5.99e-03 A/m
Tw¹_12Fb
NRM
333 C
444
533
540
604
13.5 mA/m
Mmax= 104 mA/m
Tw¹_11Aa
555
568
640
3.09 mA/m
Mmax= 17.8 mA/m
Tw¹_13Gb
NRM
120 C
366
466
560
573
594
3.12 mA/m
Mmax= 16.7 mA/m
Tw¹_16Ia
NRM
166 C
288
396
488
544
561
600
1.28 mA/m
Mmax= 7.5 mA/m
Tw¹_17Da
NRM
166 C
288
396
488
544
561
640
1.08 mA/m
Mmax= 6.1 mA/m
Tw¹_18Ba
NRM
166 C
288
396
444
488
585
1.69 mA/m
Mmax= 9.9 mA/m
Tw¹_27Da
NRM
210 C
344
466
595
1.07 mA/m
Mmax= 7.5 mA/m
Tw¹_28Ga
NRM
166 C
288
396
488
520
544
573
W E
S Dn
0.881mA/m
Mmax= 5.3 mA/m
M/Mmax
Temperature, C
Gastaldo et al.
Fig. SI 3

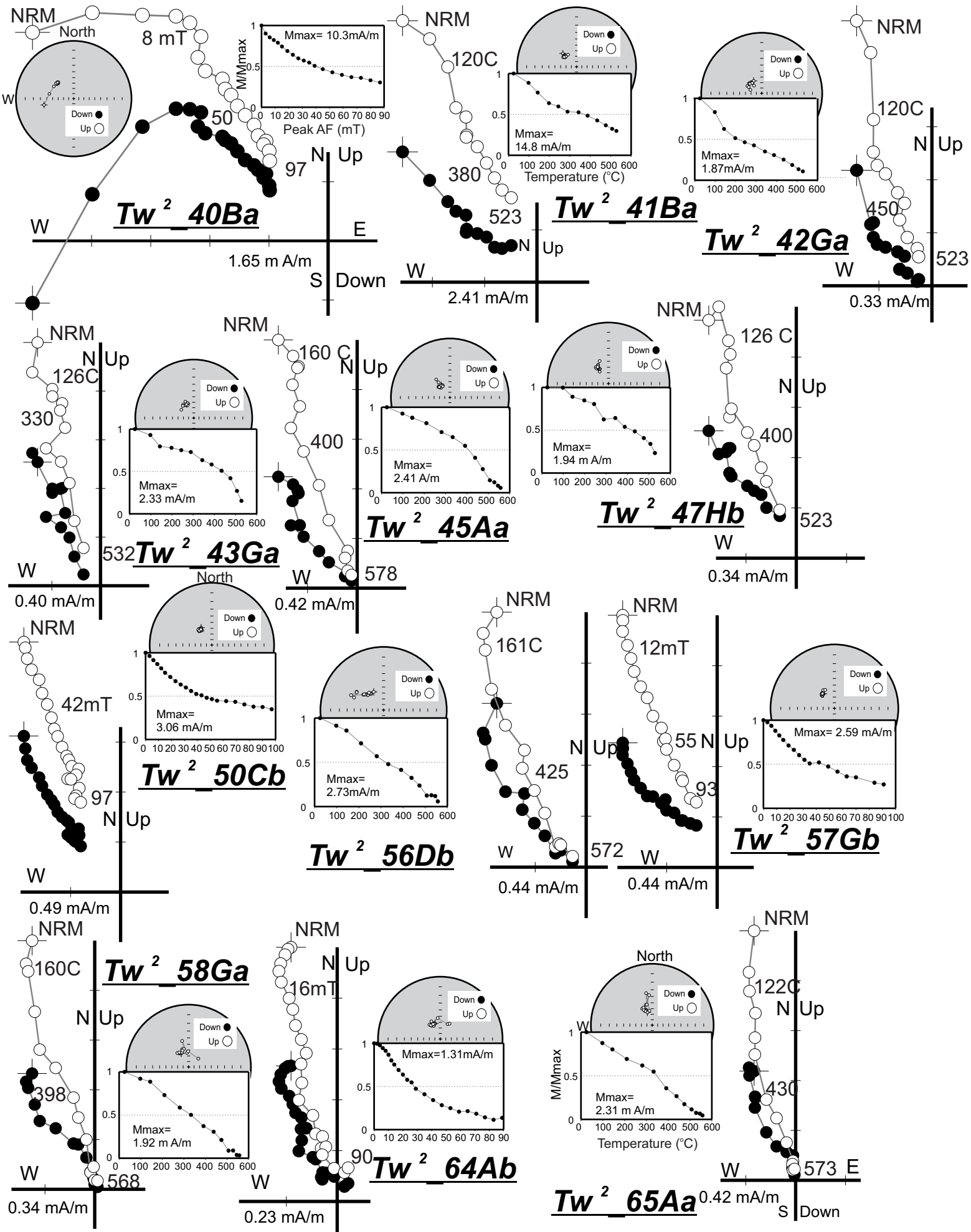

Gastaldo et al. Fig. SI 3

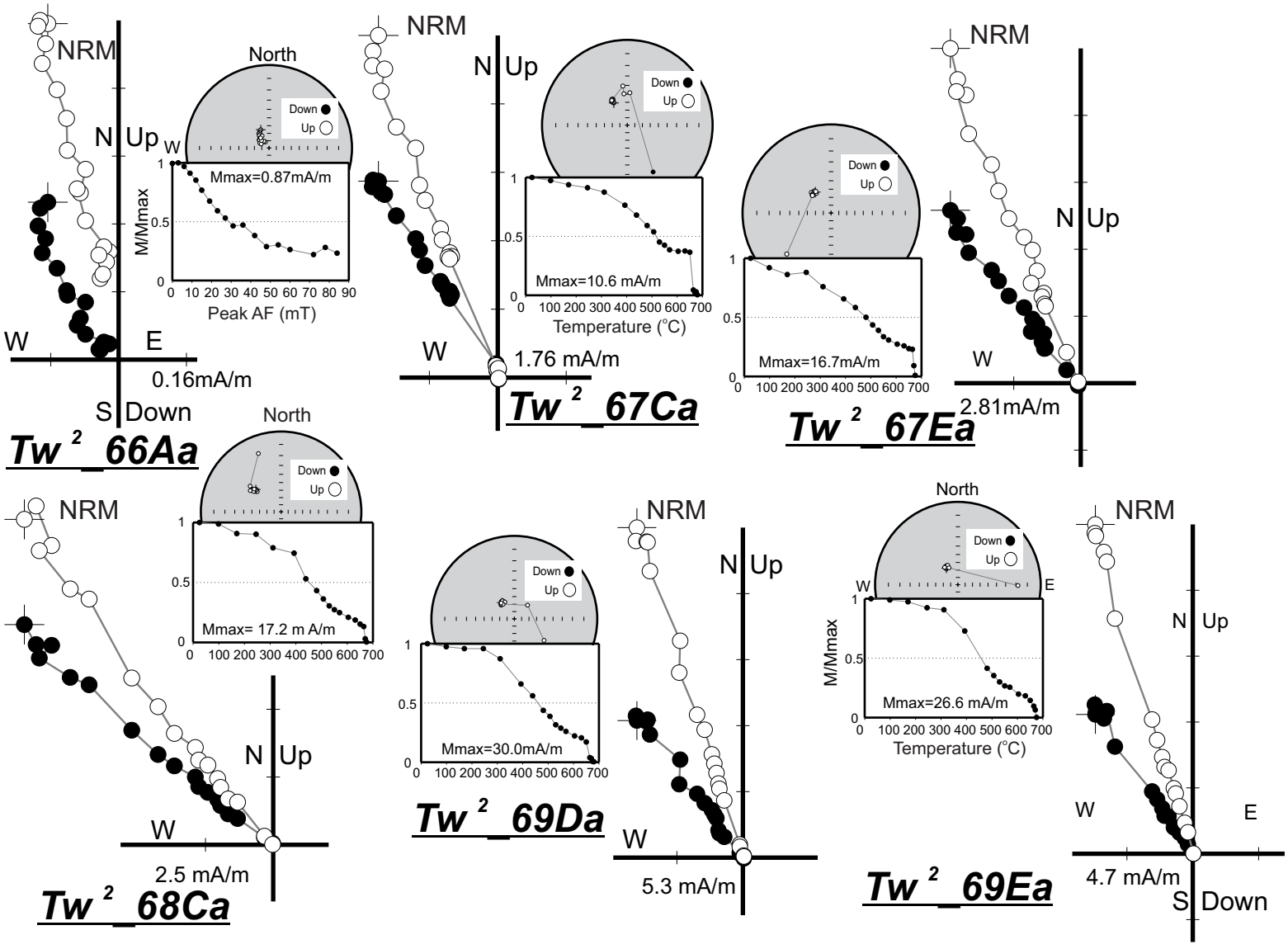

Gastaldo et al. Fig. SI 3

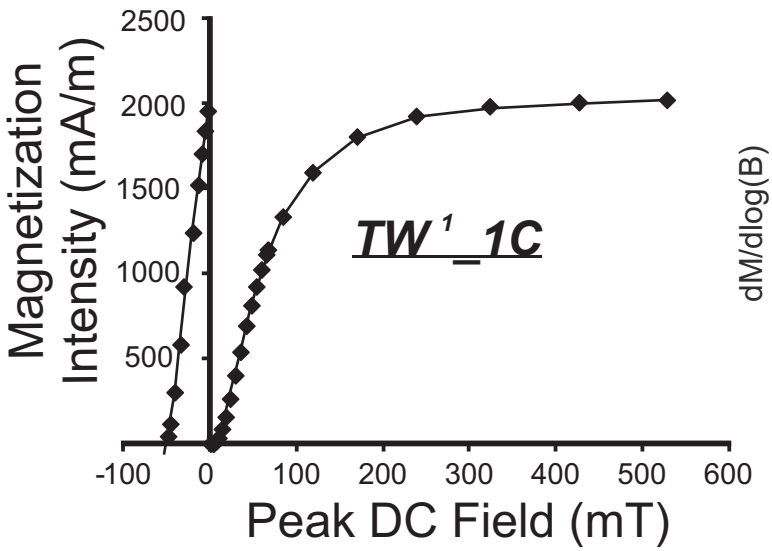

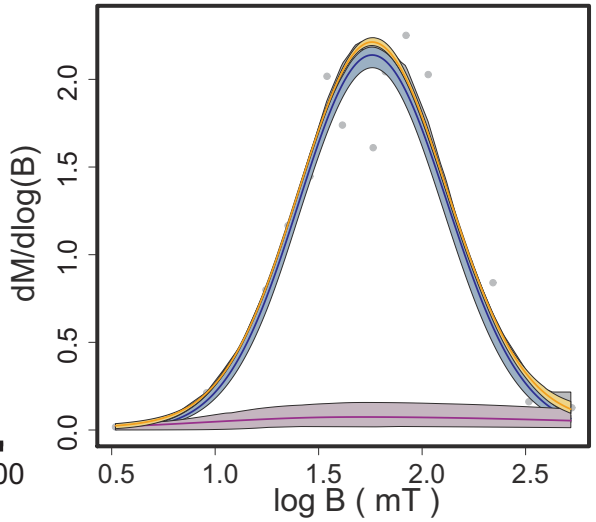

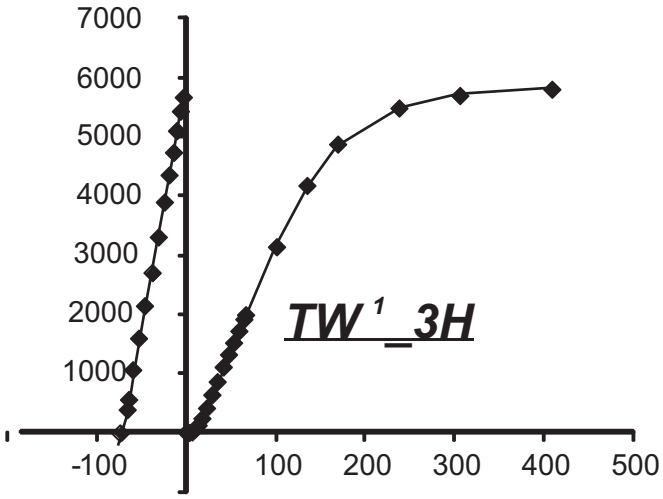

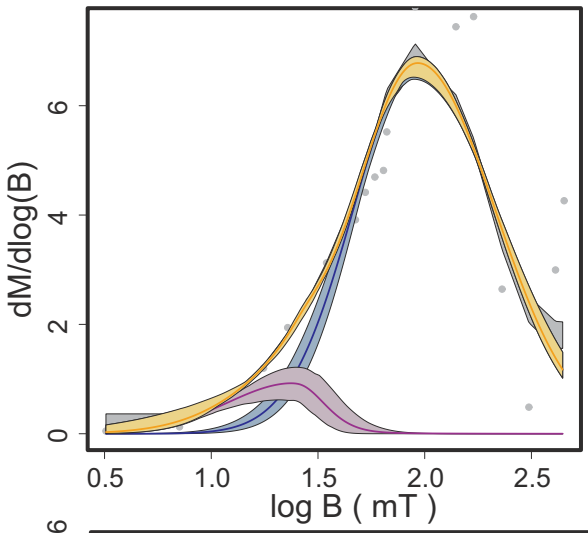

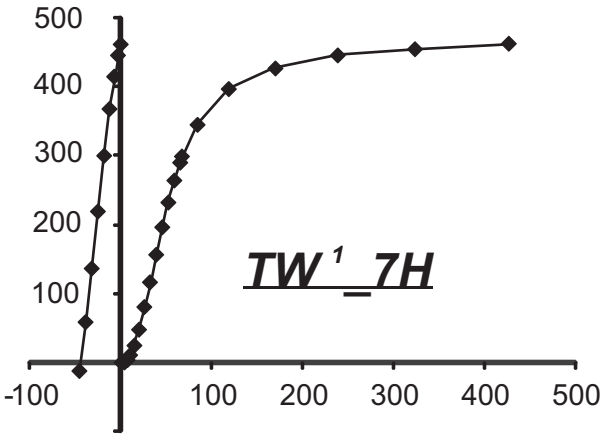

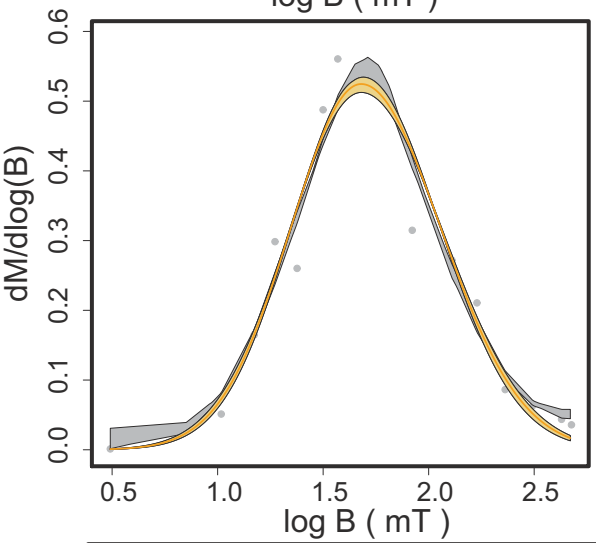

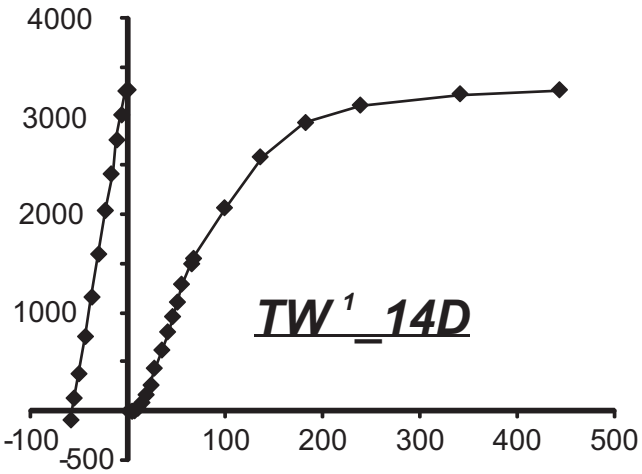

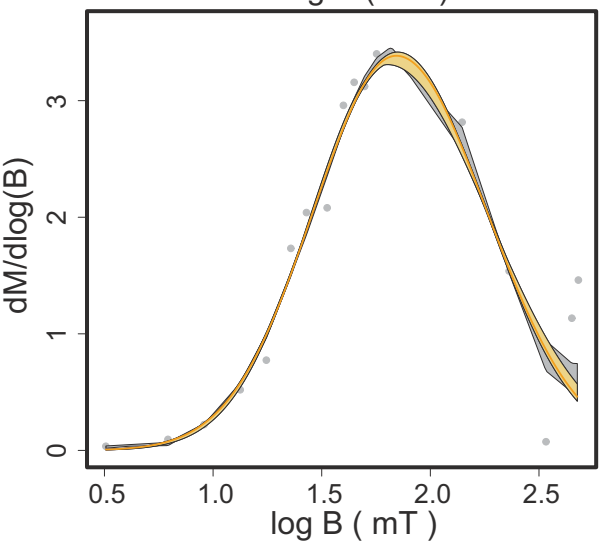

Gastaldo et al. Fig. SI4

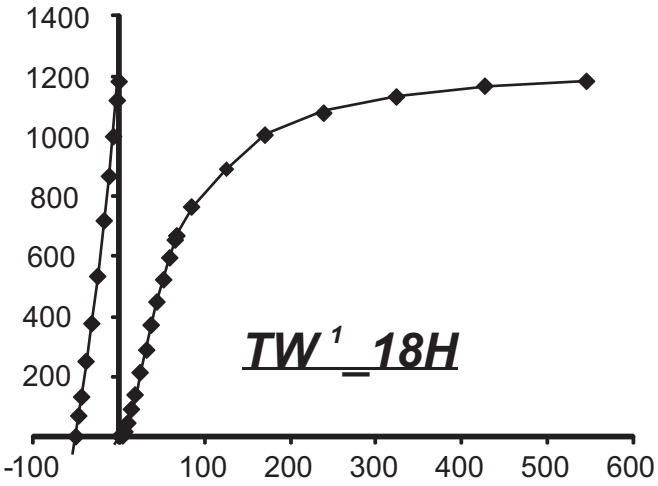

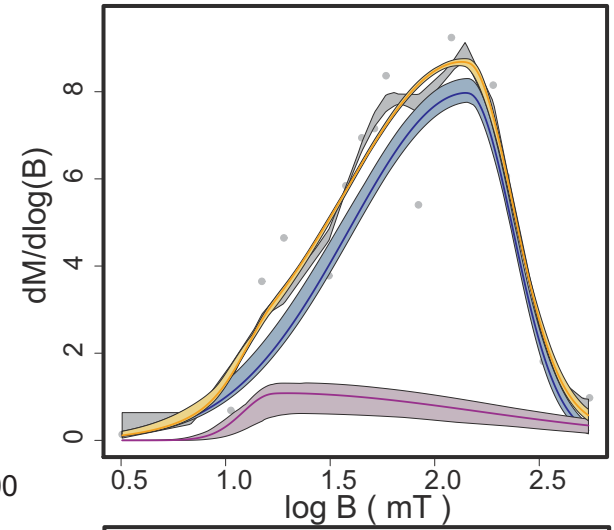

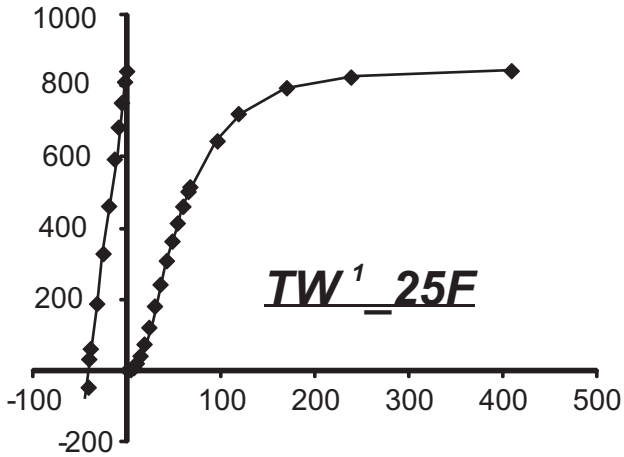

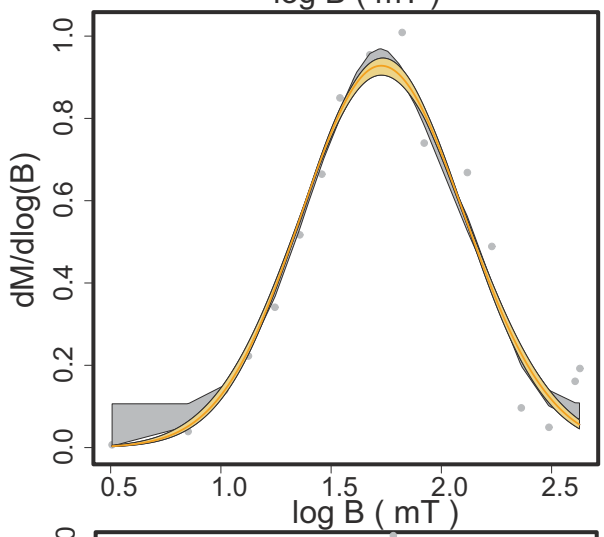

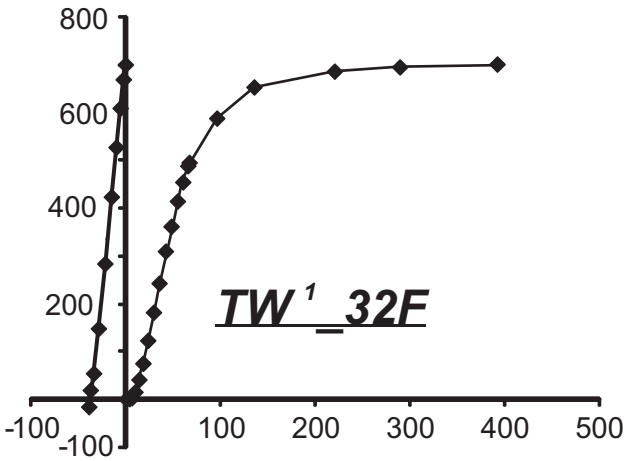

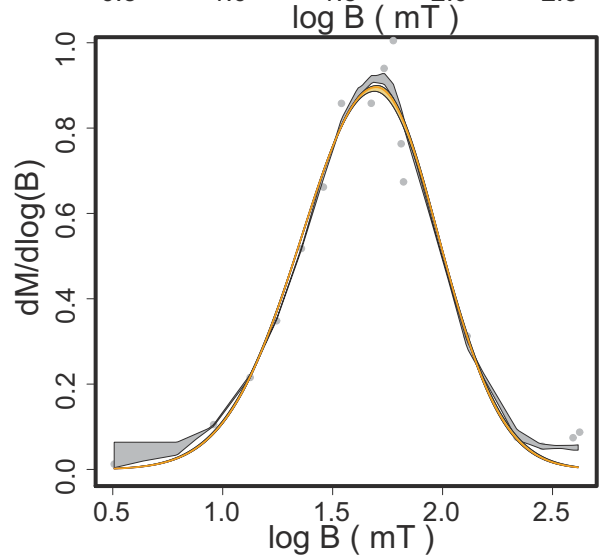

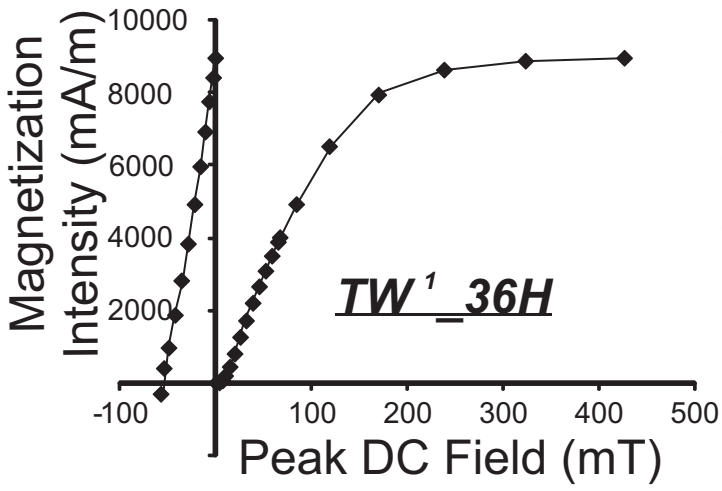

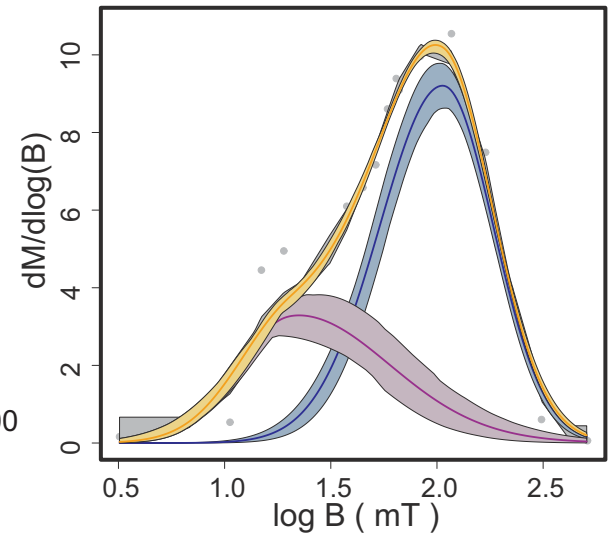

Gastaldo et al. Fig. SI4

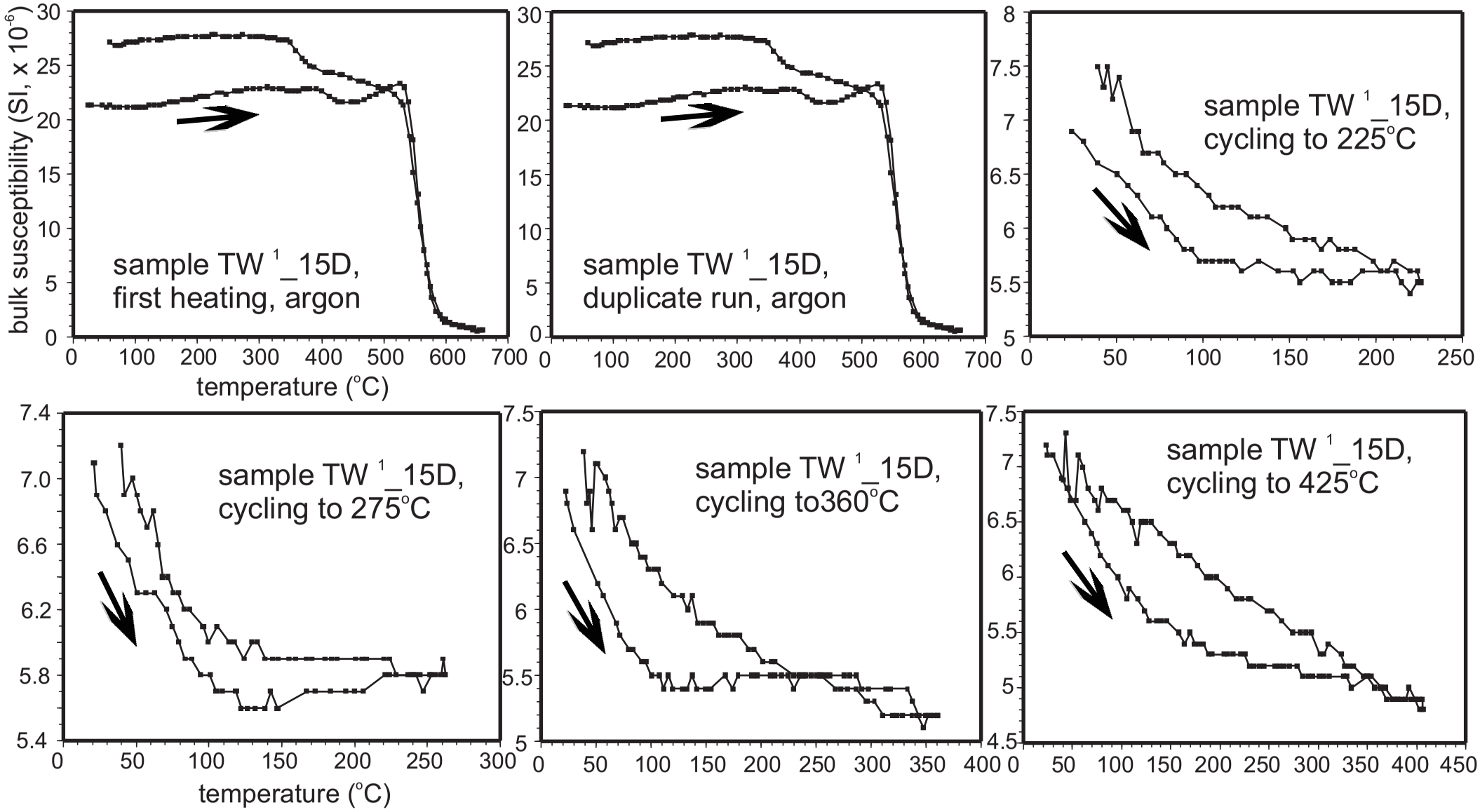

Gastaldo et al. Fig. SI5

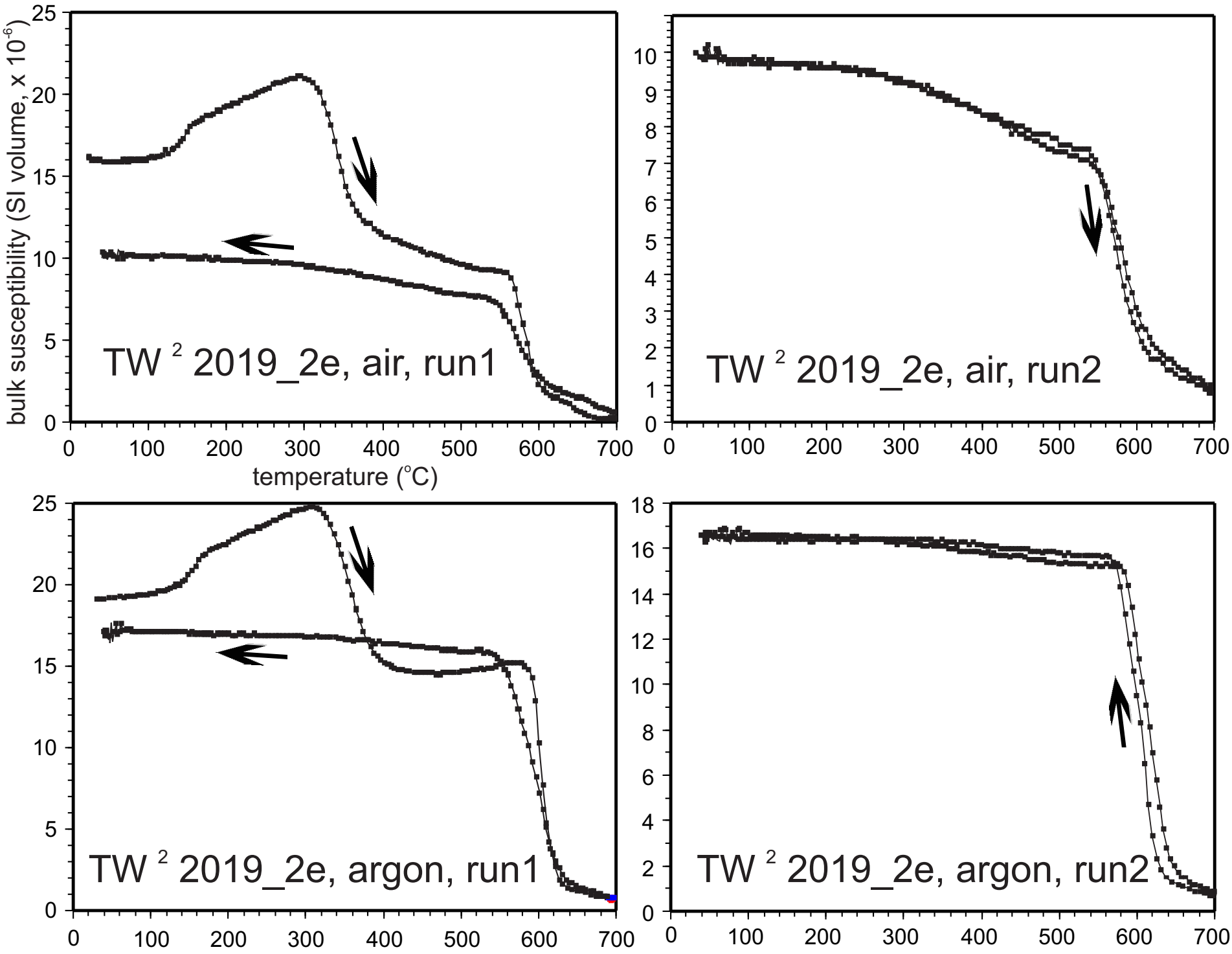

Gastaldo et al. Fig. SI6

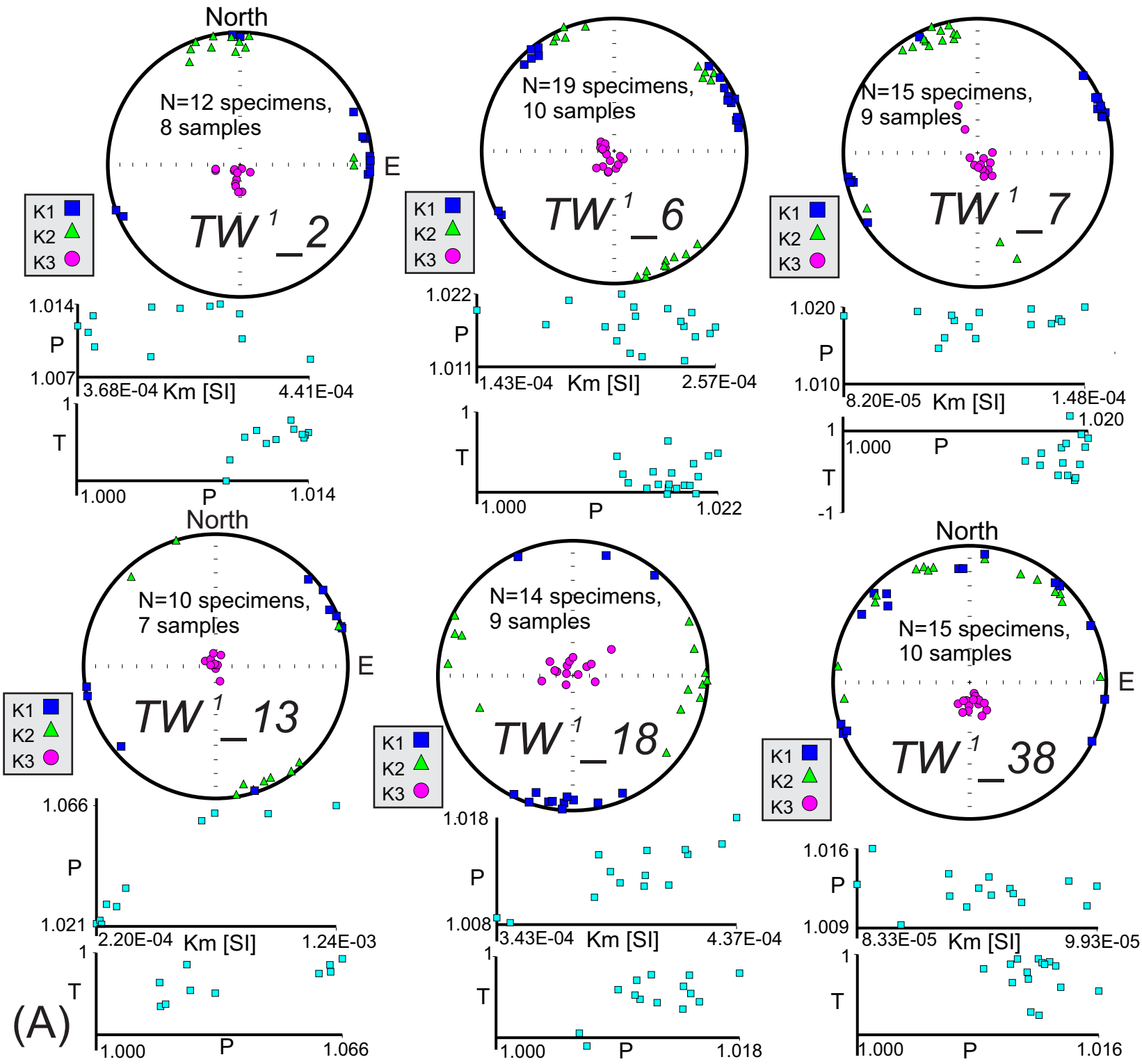

Gastaldo et al. Fig. SI7

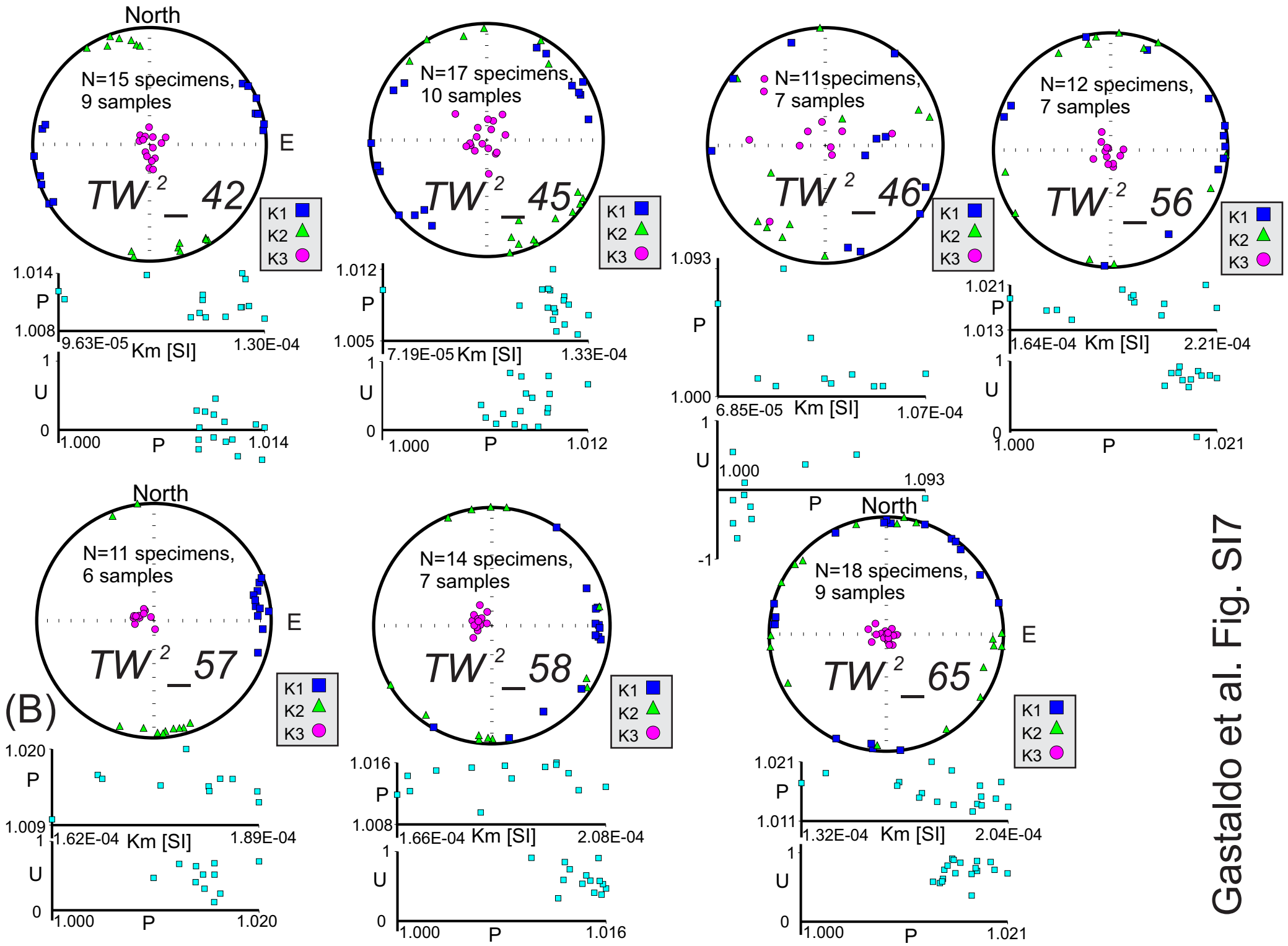
North
N=15 specimens,
9 samples
E
TW2_42
K1
K2
K3
1.014
P
1.008
9.63E-05
Km [SI]
1.30E-04
1
U
0
1.000
P
1.014
N=17 specimens,
10 samples
TW2_45
1.012
P
1.005
7.19E-05
Km [SI]
1.33E-04
1
U
0
1.000
P
1.012
N=11specimens,
7 samples
TW2_46
1.093
P
1.000
6.85E-05
Km [SI]
1.07E-04
1
U
-1
1.000
P
1.093
N=12 specimens,
7 samples
TW2_56
1.021
P
1.013
1.64E-04
Km [SI]
2.21E-04
1
U
0
1.000
P
1.021
(B)
North
N=11 specimens,
6 samples
E
TW2_57
1.020
P
1.009
1.62E-04
Km [SI]
1.89E-04
1
U
0
1.000
P
1.020
N=14 specimens,
7 samples
TW2_58
1.016
P
1.008
1.66E-04
Km [SI]
2.08E-04
1
U
0
1.000
P
1.016
North
N=18 specimens,
9 samples
E
TW2_65
1.021
P
1.011
1.32E-04
Km [SI]
2.04E-04
1
U
0
1.000
P
1.021
Gastaldo et al. Fig. SI7

Gastaldo et al. Fig. SI 8

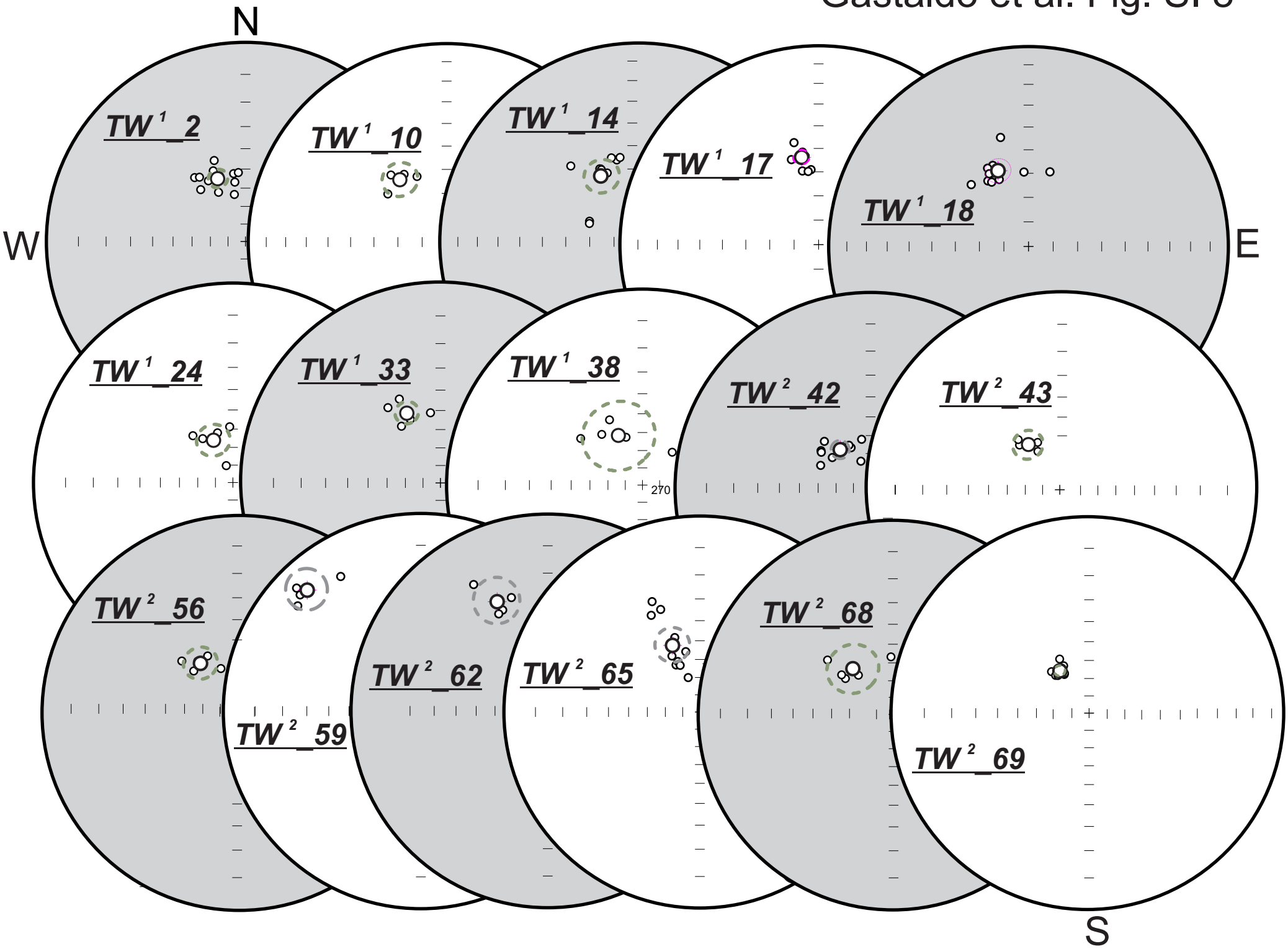

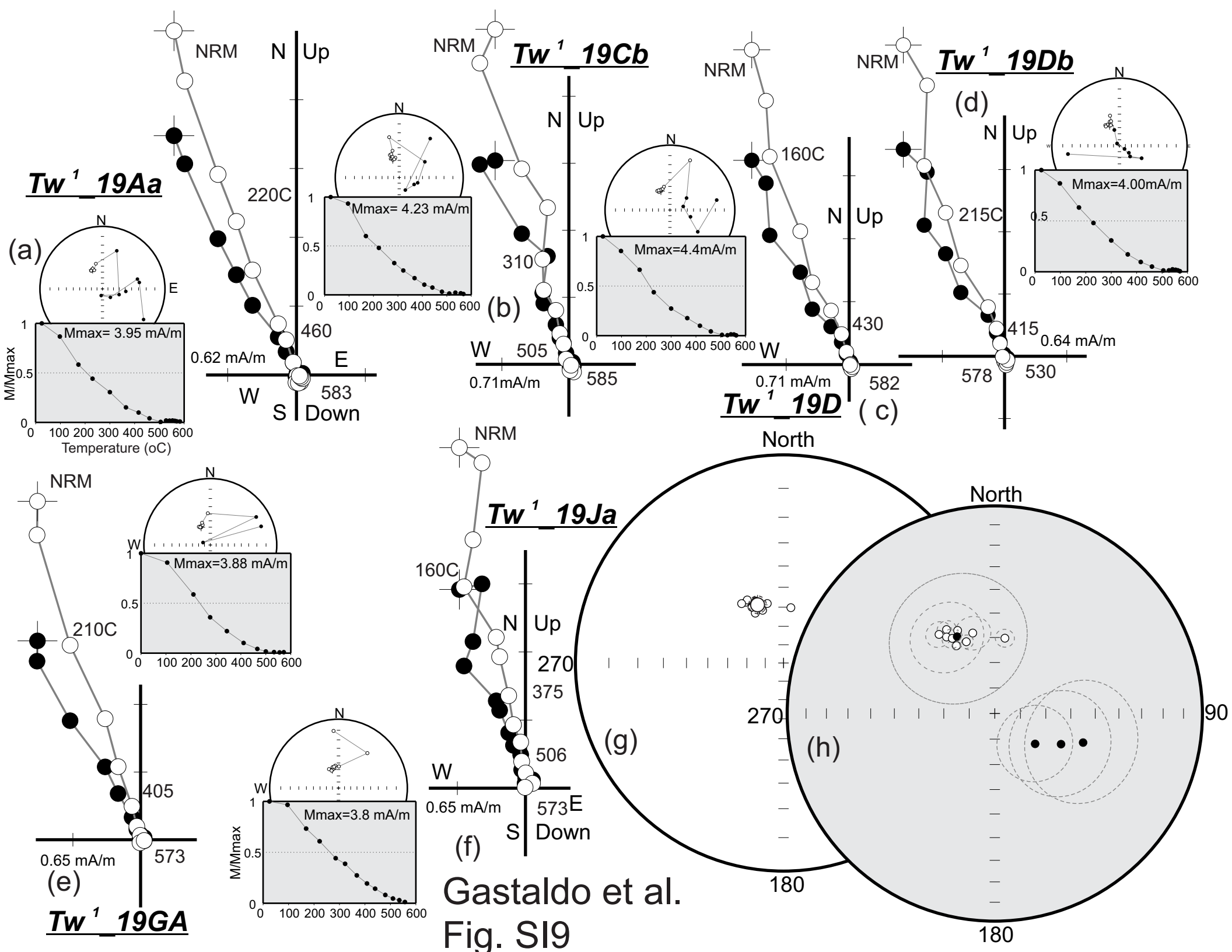
Tw¹_19Aa
NRM
N
Up
220C
460
0.62 mA/m
E
W
S
Down
583
(a)
Mmax= 3.95 mA/m
M/Mmax
Temperature (oC)
Tw¹_19Cb
NRM
N
Up
310
505
0.71mA/m
585
(b)
Mmax=4.4mA/m
Tw¹_19D
NRM
160C
430
0.71 mA/m
582
(c)
Tw¹_19Db
NRM
(d)
215C
415
0.64 mA/m
578
530
Mmax=4.00mA/m
Tw¹_19Ja
NRM
160C
270
375
506
W
0.65 mA/m
573
E
S
Down
(f)
Mmax=3.88 mA/m
Tw¹_19GA
NRM
210C
405
0.65 mA/m
573
(e)
Mmax=3.8 mA/m
M/Mmax
North
270
180
(g)
North
270
90
180
(h)
Gastaldo et al.
Fig. SI9

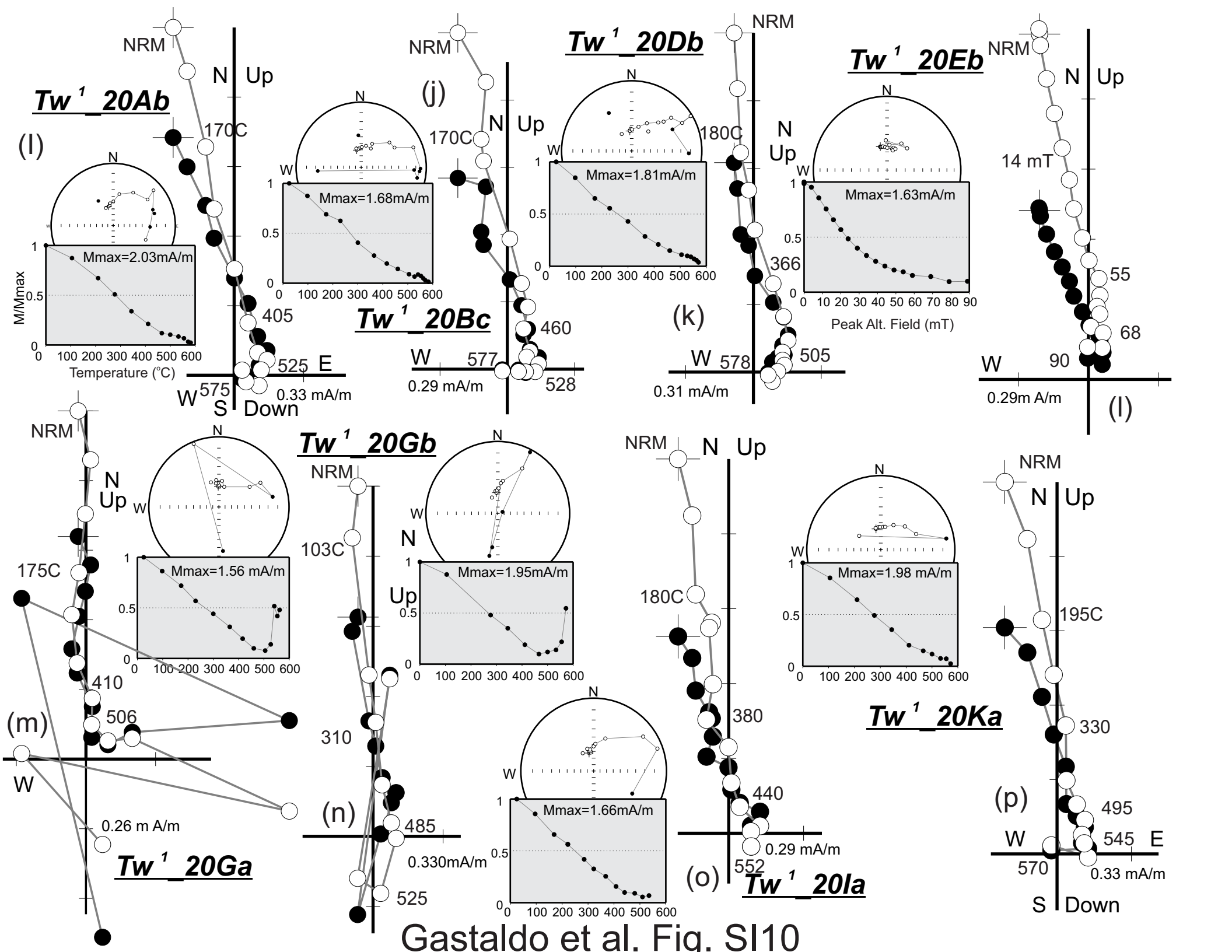

Gastaldo et al. Fig. SI10

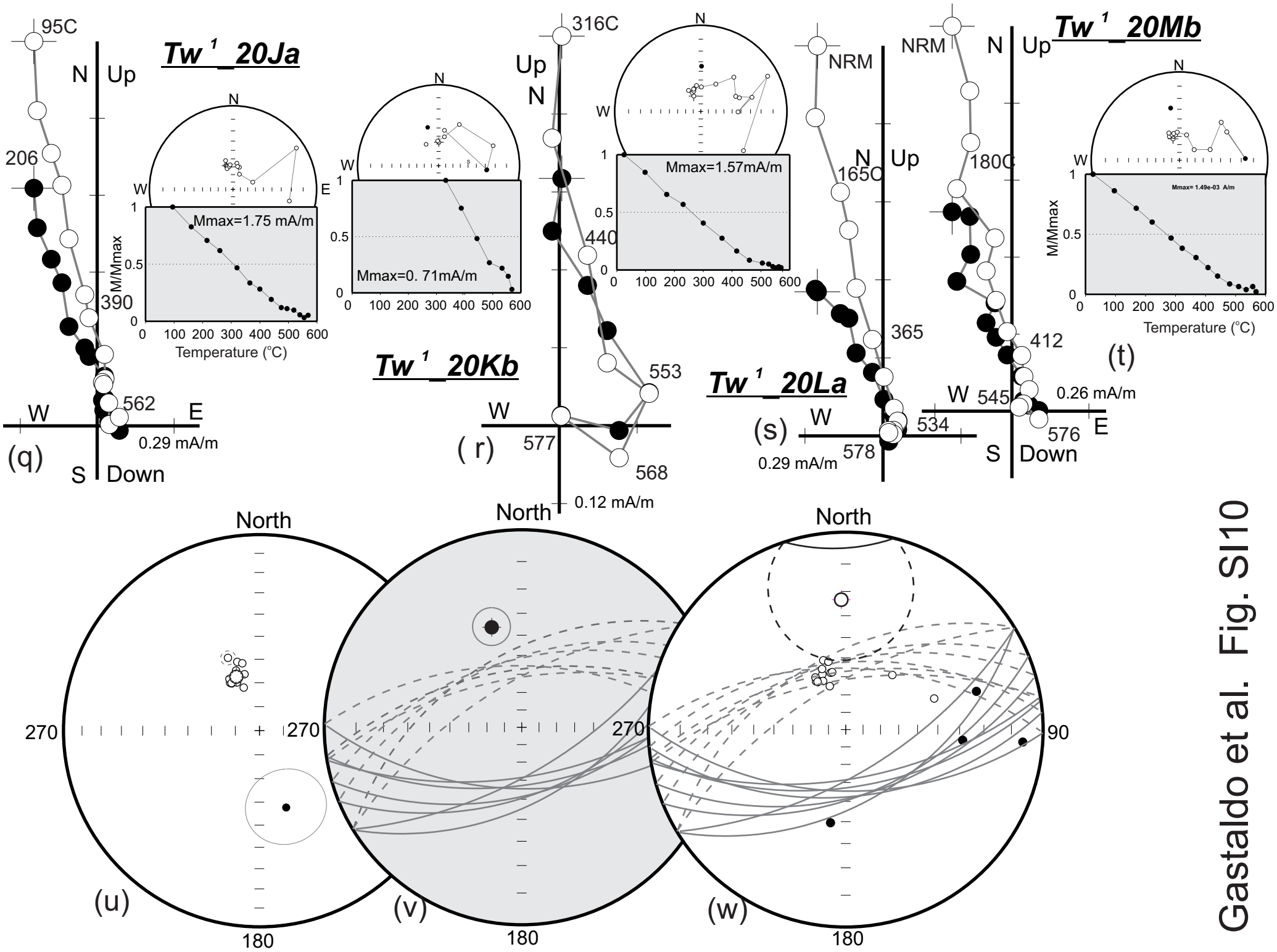
Tw¹_20Ja
Tw¹_20Kb
Tw¹_20La
Tw¹_20Mb
95C
206
390
562
N
Up
W
E
S
Down
0.29 mA/m
(q)
Mmax=1.75 mA/m
M/Mmax
Temperature (°C)
Mmax=0. 71mA/m
316C
553
577
568
0.12 mA/m
(r)
Mmax=1.57mA/m
440
NRM
165C
365
534
578
0.29 mA/m
(s)
180C
412
545
576
0.26 mA/m
(t)
Mmax= 1.49e-03 A/m
North
270
90
180
(u)
(v)
(w)
Gastaldo et al. Fig. SI10